IMMUNE REGULATION

A light-regulated circadian timer optimizes neutrophil bactericidal activity to boost daytime immunity

Lucia Yi Du[1,2,3]†, Pramuk Keerthisinghe[1,4]†, Leah Rolland[1], Yih Jian Sung[1], Hannah Darroch[1,5], Tanja Linnerz[1], Elina Ashimbayeva[1], Matthew J. Grant[6], Purvi M. Kakadia[7], Annasuya Ramachandran[1], Alexander Tups[4], Herman P. Spaink[8], Stefan K. Bohlander[7], James Cheeseman[9], Philip S. Crosier[1], Jonathan W. Astin[1], Guy Warman[9], Christopher J. Hall[1]*

The immune response exhibits strong circadian rhythmicity, with enhanced bacterial clearance often synchronized with an organism's active phase. Despite providing the bulk of cellular antibacterial defense, the neutrophil clockwork is poorly understood. Here, we used larval zebrafish to explore the role of clock genes in neutrophils during infection. *Per2* was required in neutrophils for reactive oxygen species (ROS) production and bacterial killing by enhancing infection-responsive expression of *high-mobility group box 1a* (*hmgb1a*). The Cry binding domain of Per2 was required for regulation of neutrophil bactericidal activity, and neutrophils lacking Cry1a had elevated bactericidal activity and infection-responsive *hmgb1a* expression. A conserved cis-regulatory element with BMAL1 and nuclear factor κB binding motifs gated infection-responsive *hmgb1a* expression to the light phase. Mutagenesis of the BMAL1 motif in neutrophils blunted the priming effect of light on bactericidal activity and *hmgb1a* expression. These findings identify a light-responsive cell-intrinsic timer that controls time-of-day variations in antibacterial activity.

INTRODUCTION

The circadian clock is a 2.5-billion-year-old cellular timekeeper that coordinates the activity of an organism in preparation for recurring daily environmental challenges (*1*). Host responses to bacterial infection demonstrate strong circadian rhythmicity, with peak immune responses often observed during an animal's early active phase (*2–4*). This adaptation likely evolved to synchronize elevated antibacterial immune responses with the increased threat of infection during an organism's period of activity. Genetic or environmental (e.g., shift work or jet lag) disruption of endogenous circadian rhythms leads to increased susceptibility to infections (*5*). As such, targeting the circadian clock may represent an exciting approach to fight infections (*5*).

The core of the circadian clock consists of the transcription factors CLOCK and BMAL1 (encoded by *Arntl*) that form a heterodimer and drive rhythmic expression of clock-controlled genes (CCGs). These CCGs include the other core clock components, period 2 (*Per2*) and its binding partner cryptochrome 1 (*Cry1*). Although the function of CRY1 as a repressor of CLOCK:BMAL1-driven transcription is well established, the role of PER2 is less clear, with evidence that it can both support and antagonize CRY1-mediated repression (*6–8*). Mice lacking *Clock* have been shown to lose circadian variation in their ability to clear the pathogen *Salmonella enterica*

serovar Typhimurium (*Salmonella*) (*9*). In addition, lineage-specific ablation of circadian clock components within lymphocytes, dendritic cells, and monocytes/macrophages has revealed that intrinsic circadian clocks operate within immune cells to orchestrate immune responses (*10–17*). CLOCK:BMAL1 likely cooperates with other transcription factors to drive tissue-specific rhythmic CCG expression, potentially by regulating transcriptionally permissive chromatin (*18–22*). Examination of CLOCK:BMAL1 binding sites has revealed that many have neighboring nuclear factor κB (NF-κB) binding motifs, raising the possibility that CLOCK:BMAL1 rhythmically primes NF-κB binding during inflammation or infection to initiate rhythmic immune responses (*23*). Despite it being the most abundant circulating leukocyte and providing the bulk of cellular antibacterial defense (*24*), very little is known about the neutrophil clockwork. Neutrophil trafficking throughout the body is under tight circadian control, with numbers increasing in the circulation during the resting phase (*25*, *26*). During the active phase, neutrophils migrate into peripheral tissues, where they are thought to provide enhanced immune surveillance against bacterial encounters (*27*, *28*). Whether clock components operate cell-autonomously within neutrophils to directly regulate circadian-gated bactericidal activity remains unknown.

By 2 days postfertilization (dpf), larval zebrafish are populated with neutrophils and macrophages that are functionally equivalent to those in mammals (*29–32*). Having a full complement of clock genes, zebrafish are also a popular model to study circadian biology (*33*, *34*). Our previous work has revealed that the larval zebrafish innate immune response to *Salmonella* is most potent during the active phase (daytime for diurnal zebrafish) (*35*). This phenotype coincided with elevated ubiquitous expression of the light-responsive clock genes *per2* and *cry1a* (*35*). In this work, we explore the roles of *per2* and *cry1a* during the host response to infection, focusing on neutrophil bactericidal activity. By generating larval zebrafish deficient in *per2* and *cry1a*, we reveal a cell-autonomous role for Per2 in synchronizing elevated bactericidal reactive oxygen species (ROS)

[1]Department of Molecular Medicine and Pathology, Faculty of Medical and Health Sciences, University of Auckland, Auckland, New Zealand. [2]Biozentrum, University of Basel, Basel, Switzerland. [3]Allen Discovery Center for Cell Lineage Tracing, Seattle, WA, USA. [4]Centre For Neuroendocrinology, University of Otago, Dunedin, New Zealand. [5]Department of Pathology, Dunedin School of Medicine, University of Otago, Dunedin, New Zealand. [6]Auckland, New Zealand. [7]Leukaemia & Blood Cancer Research Unit, Department of Molecular Medicine and Pathology, Faculty of Medical and Health Sciences, University of Auckland, Auckland, New Zealand. [8]Institute of Biology, Leiden University, Leiden, Netherlands. [9]Department of Anaesthesiology, School of Medicine, Faculty of Medical and Health Sciences, University of Auckland, Auckland, New Zealand.
*Corresponding author. Email: c.hall@auckland.ac.nz
†These authors contributed equally to this work.

production in neutrophils with the light phase. We demonstrate that this was by enhancing the expression of *high-mobility group box 1a* (*hmgb1a*), the zebrafish ortholog of the damage-associated molecular pattern (DAMP) *HMGB1*, and that Per2 requires its Cry binding domain to augment neutrophil function. In contrast with Per2, Cry1a antagonizes infection-responsive *hmgb1a* expression and neutrophil bactericidal activity. Providing a mechanistic connection between light, Per2, Cry1a, and *hmgb1a* expression, we show that light primes infection-responsive transcription of *hmgb1a* within neutrophils through a conserved cis-regulatory element (CRE) that has BMAL1 and NF-κB binding motifs. Moreover, targeted mutagenesis of this BMAL1 site in neutrophils suppresses light-primed expression of *hmgb1a* after infection, leading to diminished bactericidal activity and survival.

RESULTS

Per2 deficiency enhances susceptibility to bacterial infection

In our previous work, we demonstrated that 2-dpf zebrafish larvae infected during the light/active phase at ZT4 (zeitgeber time, hours after lights on) exhibit improved survival associated with enhanced bacterial clearance and increased neutrophil recruitment compared with those infected during the dark/resting phase (ZT16) (*35*). Given that *per2* expression in whole larvae peaks at ZT4 and reaches its nadir at ZT16 (*35*), we hypothesized that this light-responsive core clock gene could serve as a key mediator of the light-enhanced host response to infection. Using two single guide RNAs (sgRNAs) targeting exons 10 and 11 of *per2*, we generated a *per2* mutant zebrafish line (*per2^{nz90}*) lacking 1774 base pairs (bp) of sequence, resulting in a premature stop codon within the second Per-ARNT-Sim (PAS) domain of *per2*, a domain essential for PER2 function (fig. S1A) (*36*). The peak expression levels of *per2* (at ZT4) were significantly reduced by 3.2-fold within *per2^{nz90}* larvae (Fig. 1A), indicative of nonsense-mediated decay of mutant transcripts (*37*). To assess the impact of the deletion on circadian rhythmicity, we performed behavioral analyses by tracking the activity of individual larvae for 3 days in constant conditions after 5 days of light:dark (LD) entrainment. Per2-deficient larvae had a 1.9-fold reduction in locomotor activity in the constant LD condition but largely unaltered free-running period lengths (fig. S1, B and C), consistent with previous findings (*38*). Given that Per2 is known to transcriptionally regulate the expression of other clock genes, we quantified expression levels of selected clock genes throughout a complete LD cycle, from 120 to 148 hours postfertilization (hpf), when circadian oscillations are well established (*38*). Although some clock genes demonstrated changes in peak expression levels, overall, we observed comparable rhythmicity of expression between wild-type (WT) and *per2^{nz90}* larvae (fig. S1D).

To assess the contribution of Per2 to the host response to infection, embryos were raised in LD, constant light (LL), reversed dark:light (DL), and constant dark (DD) conditions and infected with 1000 colony-forming units (CFU) of green fluorescent protein (GFP)–expressing *Salmonella* (*Sal*-GFP) by hindbrain microinjection at 52 hpf (ZT4 and ZT16 for the LD and DL conditions, respectively) (Fig. 1B). WT larvae infected during the light phase (LD and LL conditions) showed better survival outcomes compared with those infected during the dark phase (DL and DD conditions) (Fig. 1, C to F), in keeping with our previous findings (*35*). By contrast, *per2^{nz90}* larvae displayed significantly lower survival rates when infected during the light phase (28.4 and 36.0% less survival in the LD and LL conditions, respectively) (Fig. 1, C and D). This phenotype was rescued by overexpressing *per2* mRNA within *per2^{nz90}* larvae (fig. S2, A and B). In addition, *per2* mRNA overexpression enhanced the survival of WT larvae by 36.3% when infected during the dark phase (DD condition), when endogenous levels of *per2* are low (fig. S2, A and C). Because no difference in survival was observed when comparing heterozygous *per2$^{nz90/+}$* mutants to WT larvae (Fig. 1C), we focused exclusively on examining homozygous *per2^{nz90}* larvae throughout the remainder of this study. Consistent with reduced survival, *per2^{nz90}* larvae also displayed elevated bacterial burdens (Fig. 1, G to I). Quantifying neutrophil and macrophage abundance at the hindbrain infection site using the *Tg(lyz:DsRED2)* (*31*) and *Tg(mpeg1:mCherry)* (*29*) reporter lines, respectively, revealed a significant reduction in neutrophil abundance in *per2^{nz90}* larvae [1.6- to 2.2-fold reduction between 1 and 6 hours postinfection (hpi)], whereas macrophage numbers showed only a modest decrease (fig. S2, D to G). Total neutrophil and macrophage counts in whole larvae remained unchanged (fig. S2, H and I). Tracking the migration of individual neutrophils to a more constrained infection foci (the otic vesicle) revealed that neutrophils migrated with reduced speed toward injected bacteria in *per2^{nz90}* larvae (fig. S2, J to N). Thus, *per2^{nz90}* larvae infected during the light phase phenocopy WT larvae infected in the dark, when endogenous levels of *per2* are lowest. These results strongly suggest that Per2 plays a crucial role in mediating the positive impact of light on the host response to infection.

Per2 deficiency impairs neutrophil bacterial killing capacity and ROS production

We next examined whether the reduced bacterial clearance observed in *per2^{nz90}* larvae was a result of impaired phagocyte function. Bacterial killing rate was assessed using live time-lapse confocal microscopy to quantify changes in intracellular bacterial volume over time (*39*, *40*). Under LD conditions, we infected 2-dpf WT or *per2^{nz90}* larvae expressing neutrophil or macrophage reporters at ZT4 and measured bacterial killing rates of individual neutrophils and macrophages between 3 and 4 hpi. Neutrophils within *per2^{nz90}* larvae showed significant impairment in their ability to kill intracellular bacteria, whereas killing rates of *per2^{nz90}* macrophages were unchanged (Fig. 2, A and B).

A key bactericidal mechanism used by phagocytes is nicotinamide adenine dinucleotide phosphate (NADPH) oxidase (NOX)–dependent production of ROS within phagosomes containing bacteria (*41*, *42*). Using the ROS-sensitive fluorescent probe CellROX, we next quantified ROS production in bacteria-laden cells. Neutrophils from *per2^{nz90}* larvae had reduced ROS production (8.1-fold decrease in mean CellROX fluorescence intensity), whereas macrophage ROS production was not changed (Fig. 2, C to F). To confirm that our CellROX assay measured NOX-generated ROS and to assess its contribution to neutrophil bactericidal activity, we generated crispants [first-generation (F0) mutants] for *ncf1*, which encodes a critical component of the NOX complex called p47-phox (fig. S3A) (*43*). Two independent sgRNAs efficiently edited *ncf1*, as confirmed by the T7 endonuclease I assay (fig. S3B), Sanger sequencing (fig. S3, C and D), and next-generation sequencing (NGS) (fig. S3, E to J). Neutrophils in *ncf1* crispants demonstrated significantly reduced killing rates and ROS production compared with sgRNA-only controls (fig. S3, K to O). These results suggest that the reduced ability
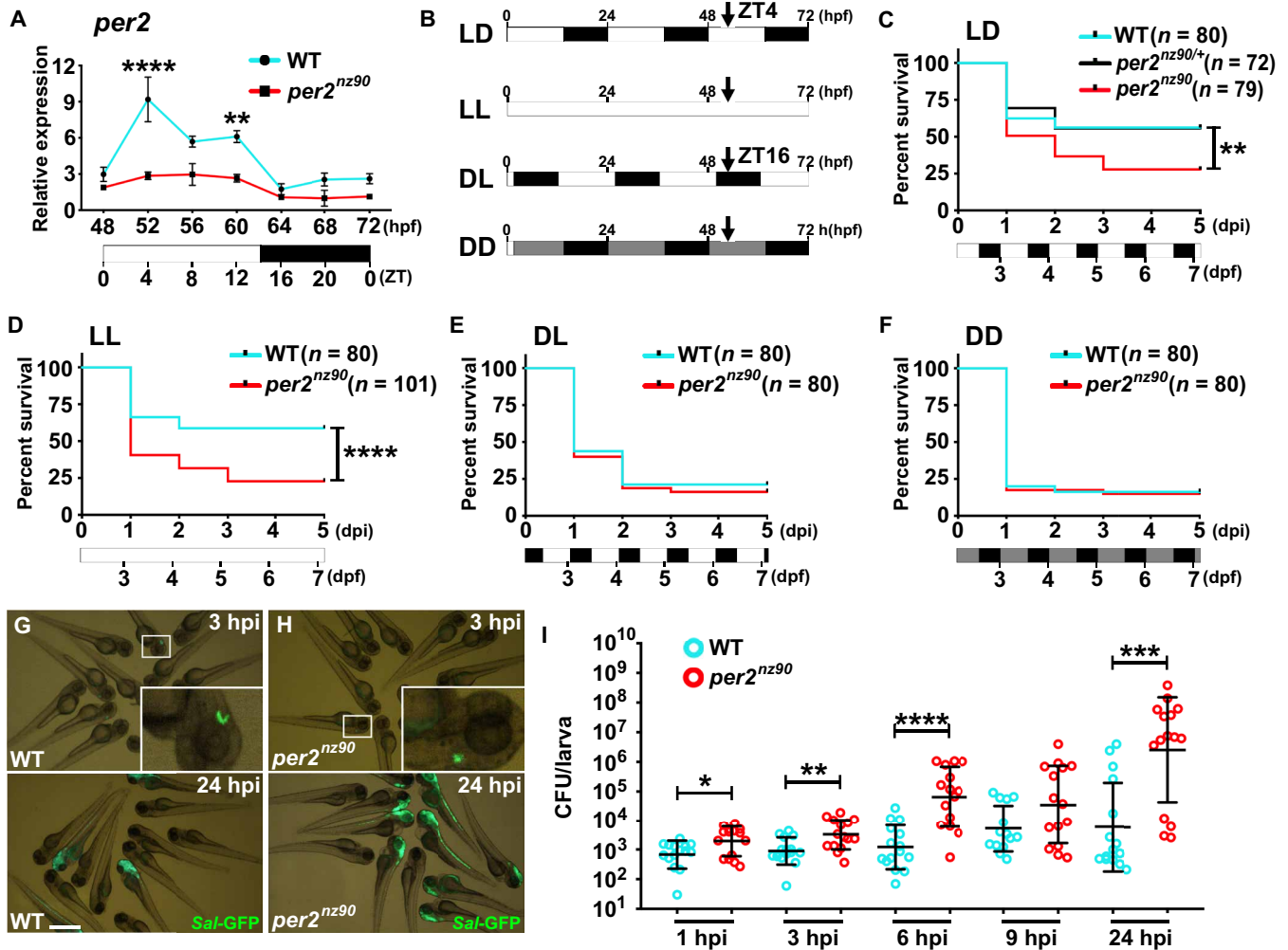
Fig. 1. Per2 deficiency enhances susceptibility to bacterial infection. (**A**) Expression of *per2* in whole WT and *per2^nz90* larvae from 48 to 72 hpf under LD conditions (qRT-PCR, *n* = 20 larvae per sample in experimental triplicate, normalized to lowest time point). (**B**) Schematic illustrating lighting conditions for infection experiments in (C) to (F), LD, LL, reversed DL, and DD, infected with *Salmonella* at 52 hpf (ZT4 and ZT16 under LD and DL conditions, respectively). (**C** to **F**) Kaplan-Meier graphs of WT, *per2^nz90/+* [(C) only] and *per2^nz90* larvae under the LD (C), LL (D), DL (E), and DD (F) conditions. (**G** and **H**) Live imaging of infected WT (G) and *per2^nz90* (H) larvae at 3 and 24 hpi with *Sal*-GFP (LD condition). Insets: Magnified views of boxed regions. Scale bar, 500 μm. (**I**) Bacterial burdens within WT and *per2^nz90* larvae at 1, 3, 6, 9, and 24 hpi with *Sal*-GFP (LD condition). Data in (C) to (F) collected from three independent experiments per sample. Error bars denote means ± SD. *P < 0.05, **P < 0.01, ***P < 0.001, and ****P < 0.0001; two-way ANOVA with Bonferroni's post test (A), Gehan-Breslow-Wilcoxon test [(C) to (F)], or unpaired Student's *t* test (I). dpi, days post infection.

of *per2^nz90* larvae to clear bacterial infections is, at least in part, the result of diminished NOX-dependent ROS production by neutrophils.

Per2 contributes to neutrophil bactericidal activity in a cell-autonomous manner

To investigate whether Per2 operates cell-autonomously to regulate neutrophil bactericidal activity, we used a previously established neutrophil transplantation protocol (*44*). Neutrophils were fluorescence-activated cell sorting (FACS)–isolated at ZT4 from 4-dpf donor *Tg(lyz:DsRED2);per2^nz90* and *Tg(lyz:DsRED2)* larvae, when DsRED2 expression was sufficiently strong to enable visualization of cells during transplantation (*39*), and transplanted into the hindbrains of age-matched *per2^nz90* and WT recipients. After a 1-day recovery period, successfully engrafted recipients were infected at ZT4, and

neutrophil killing rates and ROS production were assessed (fig. S4, A and B). This analysis revealed that *per2^nz90* neutrophils demonstrated reduced killing rates and ROS production (4.1-fold decrease in mean CellROX fluorescence intensity) within a WT background (Fig. 3, A and B). By contrast, transplanted WT neutrophils had comparable bactericidal activity when imaged within *per2^nz90* and WT backgrounds.

From our transplantation experiments, we hypothesized that rescuing *per2* expression specifically in neutrophils of *per2^nz90* larvae would restore bactericidal function. We generated a neutrophil-specific *per2* rescue line *Tg(lyz:DsRED2);Tg(lyz:per2);per2^nz90* (fig. S4C), which restored *per2* expression to peak WT levels within *per2^nz90* neutrophils (Fig. 3C). The rescue line demonstrated survival comparable to that of WT larvae when infected with *Salmonella* at ZT4 under the LD condition (Fig. 3D and fig. S4D). Furthermore,
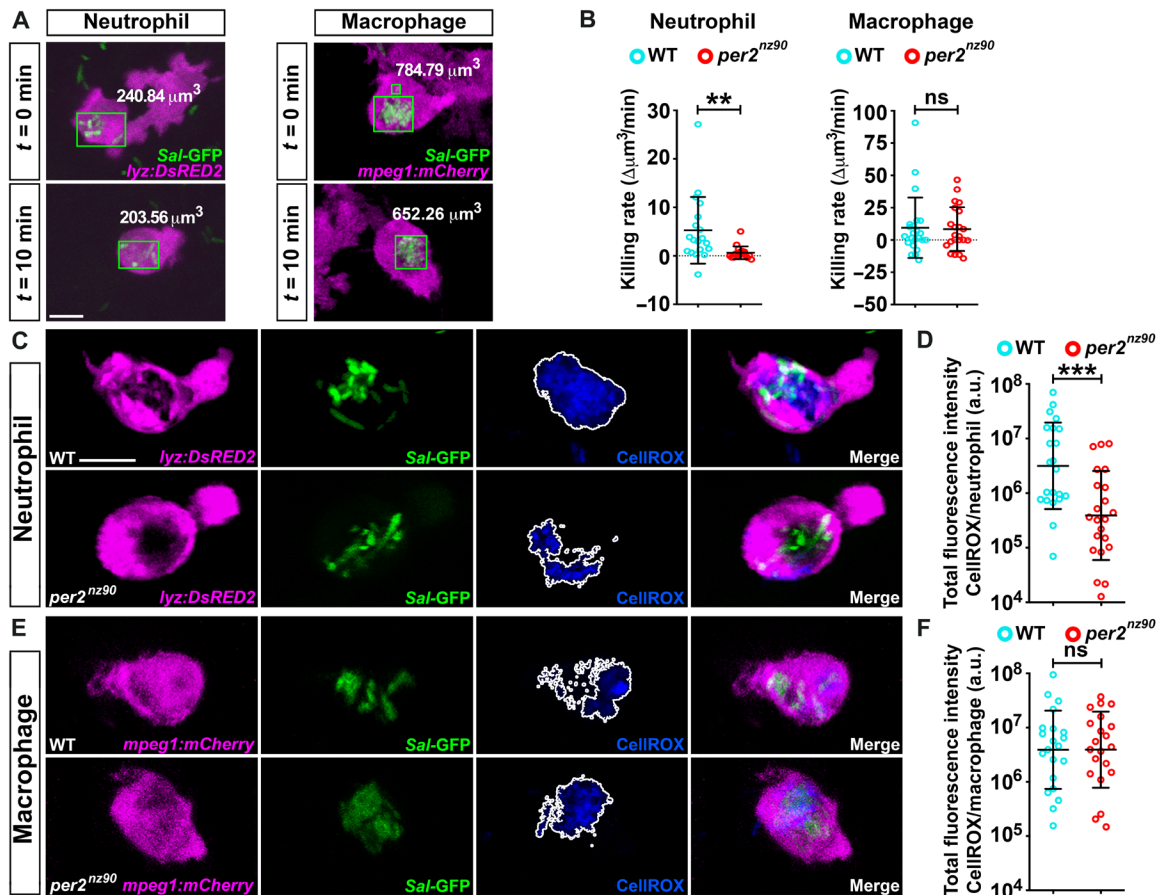
Fig. 2. Per2 deficiency impairs neutrophil bacterial killing capacity and ROS production. (**A**) Example frame shots from time-lapse confocal imaging of neutrophils and macrophages within *Tg(lyz:DsRED2)* and *Tg(mpeg1:mCherry)* larvae, respectively, showing volumes of intracellular *Sal*-GFP at the beginning ($t = 0$ min) and end ($t = 10$ min) of a time-lapse movie, captured between 3 and 4 hpi. (**B**) Bacterial killing rates of WT and *per2*^{nz90} neutrophils within *Tg(lyz:DsRED2)* and *Tg(lyz:DsRED2);per2*^{nz90} larvae, respectively, and WT and *per2*^{nz90} macrophages within *Tg(mpeg1:mCherry)* and *Tg(mpeg1:mCherry);per2*^{nz90} larvae, respectively, as imaged in (A). (**C**) Live imaging of ROS within individual *Sal*-GFP–laden WT and *per2*^{nz90} neutrophils, as detected by CellROX fluorescence (white outline). (**D**) ROS quantification, as detected in (C). (**E**) Live imaging of ROS within individual *Sal*-GFP–laden WT and *per2*^{nz90} macrophages, as detected by CellROX fluorescence (white outline). (**F**) ROS quantification, as detected in (E). Data in (B) were collected from three independent experiments per sample ($n = 6$ time-lapse movies per experiment), and data in (D) and (F) were collected from three independent experiments per sample. Error bars denote means ± SD; ns, not significant, $**P < 0.01$, and $***P < 0.001$; unpaired Student's t test. Scale bars, 10 μm in (A) and (C).

infected *Tg(lyz:DsRED2);Tg(lyz:per2);per2*^{nz90} larvae exhibited 17.1% better survival rates than WT larvae under the DD condition, when endogenous *per2* levels are low (Fig. 3E and fig. S4D). Whole-larvae neutrophil numbers remained unaltered within *Tg(lyz:DsRED2);Tg (lyz:per2);per2*^{nz90} larvae (fig. S4E). Evaluation of neutrophil killing rates and ROS production after infection under the LD condition revealed that neutrophil-restricted rescue of *per2* expression restored bactericidal activity of *per2*^{nz90} neutrophils (Fig. 3, F and G). However, this rescue line did not restore the neutrophil recruitment defect in *per2*^{nz90} larvae (fig. S4F). These results confirm that Per2 is cell-autonomously required for neutrophil bactericidal activity and suggest that *per2* expression in another tissue compartment contributes to the neutrophil migration defect.

Per2 contributes to neutrophil bactericidal activity by enhancing infection-responsive *hmgb1a* expression

Given that Per2 functions as a transcriptional regulator, we next analyzed *per2*^{nz90} neutrophil transcriptomes at steady-state (SS) and

after *Salmonella* infection. Bulk RNA sequencing (RNA-seq) was performed on WT and *per2*^{nz90} neutrophils, FACS-isolated from phosphate-buffered saline (PBS-SS)– and *Sal*-GFP–injected *Tg(lyz: DsRED2)* and *Tg(lyz:DsRED2);per2*^{nz90} larvae, respectively. In line with our live-imaging experiments, infections were delivered at 52 hpf (ZT4), and cells were harvested at 3 hpi (fig. S5A). We examined differentially expressed genes (DEGs) between WT and *per2*^{nz90} neutrophils both at SS and after infection (Fig. 4A). Gene Ontology (GO) analysis on the 253 DEGs down-regulated in *per2*^{nz90} neutrophils, which were exclusive to the infected state, revealed no significantly enriched biological processes. However, we identified *hmgb1a*, which has a well-established role as a regulator of immune responses during infectious disease (*45*), as one of the most significantly down-regulated genes (Fig. 4B and fig. S5B). Quantitative reverse transcription polymerase chain reaction (qRT-PCR) analysis confirmed that *hmgb1a* expression was elevated 11.8-fold in WT neutrophils after infection, but not in *per2*-deficient neutrophils (Fig. 4C). Furthermore, the rescue of *per2* expression within *per2*^{nz90} neutrophils
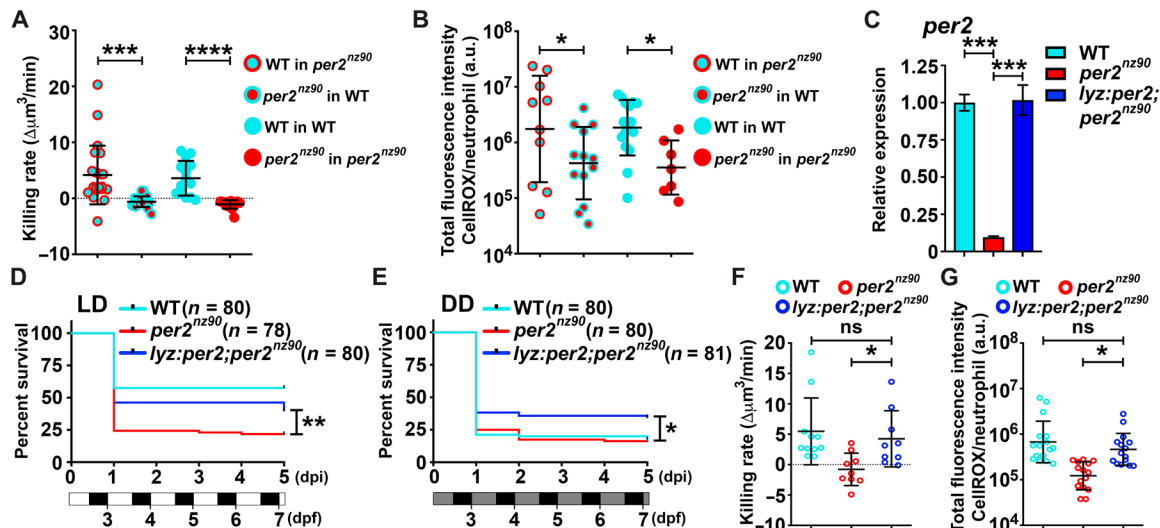
Fig. 3. Per2 contributes to neutrophil bactericidal activity in a cell-autonomous manner. (**A** and **B**) Bacterial killing rates of (A) and ROS quantification within (B) *Sal*-GFP–laden WT or *per2^{nz90}* neutrophils transplanted into WT or *per2^{nz90}* recipient larvae (data collected from ≥6 individual engrafted larvae per sample). (**C**) Expression of *per2* within neutrophils FACS-isolated from 2-dpf *Tg(lyz:DsRED2)*, *Tg(lyz:DsRED2);per2^{nz90}*, and *Tg(lyz:DsRED2);Tg(lyz:per2);per2^{nz90}* larvae at ZT4 (qRT-PCR, three experimental replicates per sample), normalized to WT group. (**D** and **E**) Kaplan-Meier graphs of *Tg(lyz:DsRED2)*, *Tg(lyz:DsRED2);per2^{nz90}*, and *Tg(lyz:DsRED2);Tg(lyz:per2);per2^{nz90}* larvae under LD (D) and DD (E) conditions after *Salmonella* infection, up to 5 dpi. (**F** and **G**) Bacterial killing rates of (F) and ROS quantification within (G) *Sal*-GFP–laden neutrophils within *Tg(lyz:DsRED2)*, *Tg(lyz:DsRED2);per2^{nz90}*, and *Tg(lyz:DsRED2);Tg(lyz:per2);per2^{nz90}* larvae (LD condition). Data in (D), (E), and (G) were collected from three independent experiments per sample, and data in (F) were collected from two independent experiments per sample (n = 6 time-lapse movies per experiment). Error bars denote means ± SD [(A), (B), (F), and (G)] or means ± SEM (C); *P < 0.05, **P < 0.01, ***P < 0.001, and ****P < 0.0001; unpaired Student's *t* test [(A) and (B)], one-way ANOVA with Dunnett's multiple comparisons test [(C), (F), and (G)], or Gehan-Breslow-Wilcoxon test [(D) and (E)].

restored infection-responsive *hmgb1a* expression to near WT levels (Fig. 4C). We did not observe infection-induced expression of *hmgb1a* within *Tg(mpeg1:EGFP)* macrophages at the same time point postinfection, in contrast with *irg1*, a gene known to augment macrophage bactericidal activity (fig. S5C) (*46*). In addition, infection had no impact on neutrophil or macrophage *per2* expression levels (fig. S5D).

Supporting a bactericidal function for Hmgb1a, morpholino (MO)–mediated depletion of Hmgb1a reduced survival (27.5% decrease in survival compared with controls) after infection, neutrophil killing rates, and ROS production (2.2-fold decrease in mean CellROX fluorescence intensity) (fig. S5, E to H). We conditionally inactivated Hmgb1a specifically in neutrophils using a *Tg(lyz:nls-cas9)* line for neutrophil-specific *cas9* expression that also expresses the lens transgenesis marker *cry:GFP* (*47*). An sgRNA targeting exon 2 of *hmgb1a* that successfully edited *hmgb1a* in whole larvae (fig. S5, I and J) also achieved selective editing within neutrophils of injected larvae (fig. S5, K to N). FACS-isolated neutrophils from 2-dpf sgRNA-injected *Tg(lyz:nls-cas9);Tg(lyz:DsRED2)* larvae revealed an editing efficiency of 41.84% (Fig. 4D and fig. S5O). By contrast, GFP+ lens cells (not expressing *cas9*) exhibited 0.07% modified alleles (Fig. 4E), similar to noninjected *Tg(lyz:nls-cas9);Tg(lyz:DsRED2)* neutrophils (fig. S5P) and whole WT larvae (fig. S5Q). We then investigated the impact of neutrophil-specific Hmgb1a inactivation on the host response to infection (fig. S5R). To evaluate any effects of *nls-cas9* expression and sgRNA injection on neutrophil function, noninjected *Tg(lyz:nls-cas9);Tg(lyz:DsRED2)* and sgRNA-injected *Tg(lyz:DsRED2)* larvae served as controls. Similar to *per2^{nz90}* larvae, neutrophil-restricted mutagenesis of *hmgb1a* resulted in reduced

survival after infection [18.5% decrease in survival compared with noninjected *Tg(lyz:DsRED2)* controls] (Fig. 4F), diminished neutrophil killing rates (Fig. 4G), and ROS production [8.9-fold decrease in mean CellROX fluorescence intensity compared with noninjected *Tg(lyz:DsRED2)* controls] (Fig. 4H). Neutrophil-specific editing of *hmgb1a* had no impact on whole-larvae neutrophil abundance (fig. S5S). To control for any unexpected impact of editing on neutrophil bactericidal function, we repeated the above analysis after neutrophil-restricted editing of *tyrosinase* (*tyr*), a gene involved in melanin development (*48*) and previously used as a negative control sgRNA when examining neutrophil function (*49*). In contrast with *hmgb1a* inactivation, *tyr* editing in neutrophils had no effect on neutrophil killing rates (fig. S6, B to G). Further supporting the specificity of the *Tg(lyz:nls-cas9)* line, no editing of *hmgb1a* was observed within macrophages isolated from the dissected trunks of *hmgb1a* sgRNA-injected *Tg(lyz:nls-cas9);Tg(lyz:DsRED2);Tg(mpeg1:EGFP)* larvae (fig. S6, H to J).

To investigate whether forced expression of *hmgb1a* within Per2-deficient neutrophils could rescue survival and bactericidal activity, we created a *Tg(lyz:DsRED2);Tg(lyz:hmgb1a);per2^{nz90}* line (fig. S6K) in which neutrophil *hmgb1a* expression levels were elevated 35.3-fold compared with *per2^{nz90}* neutrophils (fig. S6L). Similar to rescuing *per2* expression within *per2^{nz90}* neutrophils (Fig. 3, C to G), *Tg(lyz:DsRED2);Tg(lyz:hmgb1a);per2^{nz90}* larvae had a 20.9% increase in survival after infection (Fig. 4I) and elevated neutrophil killing rates (Fig. 4J) when compared with *Tg(lyz:DsRED2);per2^{nz90}* larvae despite having unaltered neutrophil abundance (fig. S6M). Thus, Per2 cell autonomously amplifies neutrophil bactericidal activity, at least in part, through positively regulating infection-responsive *hmgb1a* expression.
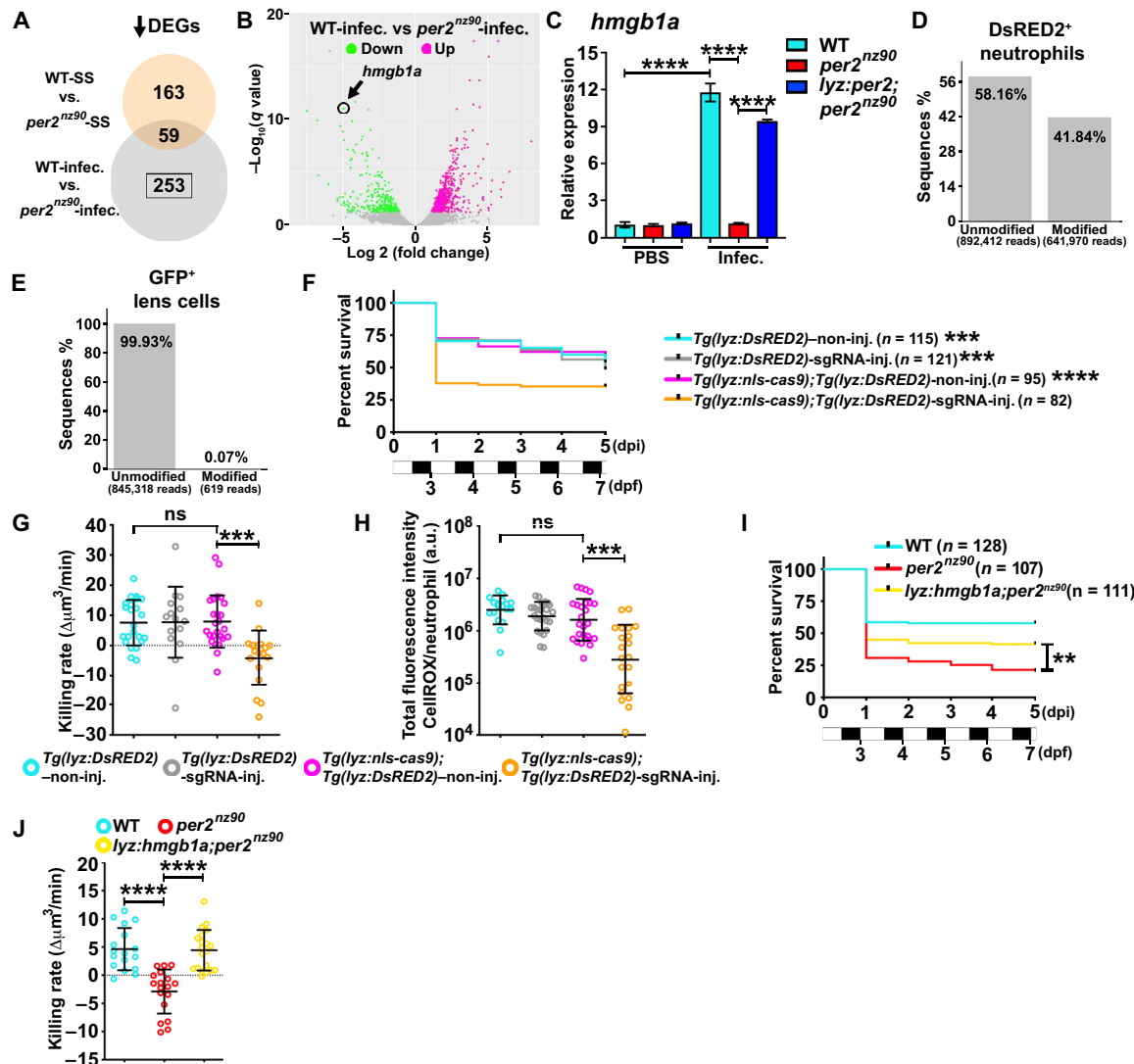
Fig. 4. Per2 positively regulates bactericidal *hmgb1a* expression. (**A**) Venn diagram showing the number DEGs down-regulated in *per2^nz90* neutrophils for the comparisons shown. The black box highlights DEGs of interest. (**B**) Volcano plot showing DEGs of interest with *hmgb1a* highlighted. (**C**) Expression of *hmgb1a* within neutrophils FACS-isolated as in (A) [including *Tg(lyz:DsRED2);Tg(lyz:per2);per2^nz90* larvae], normalized to the PBS WT group (qRT-PCR, three experimental replicates per sample). (**D** and **E**) Frequencies of unmodified and modified alleles, as detected by NGS, from neutrophils (D) and lens cells (E) FACS-isolated from *hmgb1a* sgRNA-injected *Tg(lyz:nls-cas9);Tg(lyz:DsRED2)* larvae at 2 dpf. (**F**) Kaplan-Meier graph of noninjected and *hmgb1a* sgRNA-injected *Tg(lyz:DsRED2)* and *Tg(lyz:nls-cas9);Tg(lyz:DsRED2)* larvae under LD conditions after *Salmonella* infection, up to 5 dpi [significance values shown are compared with the *Tg(lyz:nls-cas9);Tg(lyz:DsRED2)*-sgRNA-injected group]. (**G** and **H**) Bacterial killing rates of (G) and ROS quantification within (H) *Sal*-GFP–laden neutrophils within noninjected and *hmgb1a* sgRNA-injected *Tg(lyz:DsRED2)* and *Tg(lyz:nls-cas9);Tg(lyz:DsRED2)* larvae. (**I**) Kaplan-Meier graph of *Tg(lyz:DsRED2)*, *Tg(lyz:DsRED2);per2^nz90*, and *Tg(lyz:DsRED2);Tg(lyz:hmgb1a);per2^nz90* larvae under LD conditions after *Salmonella* infection up to 5 dpi. (**J**) Bacterial killing rates of neutrophils within *Tg(lyz:DsRED2)*, *Tg(lyz:DsRED2);per2^nz90*, and *Tg(lyz:DsRED2);Tg(lyz:hmgb1a);per2^nz90* larvae (LD condition). Data in (F), (H), and (I) were collected from three independent experiments per sample, and data in (G) and (J) were collected from three independent experiments per sample (*n* = 6 time-lapse movies per experiment). Error bars denote means ± SEM (C) or means ± SD [(G), (H), and (J)]; ****P* < 0.01, ***P* < 0.001, and ****P* < 0.0001; one-way ANOVA with Dunnett's multiple comparisons test [(C), (G), (H), or (J)] or Gehan-Breslow-Wilcoxon test [(F) and (I)].

Per2 overexpression in neutrophils enhances survival and bactericidal activity

We next explored the impact of light on *per2* expression in neutrophils and neutrophil bactericidal activity. First, we quantified *per2* expression in SS neutrophils under LL and DD conditions, aiming to maximize the impact of light. *Per2* expression in neutrophils was elevated 2.9-fold under the LL condition, as assessed by qRT-PCR of FACS-isolated cells (Fig. 5A), as reported for whole larvae (*35*). In contrast, *hmgb1a* expression remained unaltered (fig. S7A). Next, we assessed neutrophil bacterial killing rates, ROS production, and *hmgb1a* expression under the same lighting conditions after infection. When compared with the DD condition, neutrophil killing rates, ROS production (9.0-fold increase in mean CellROX fluorescence intensity), and *hmgb1a* expression (6.8-fold increase) were elevated under the LL condition (Fig. 5, B to D). Furthermore, infecting a stable line overexpressing *hmgb1a* within otherwise WT neutrophils

Fig. 5. Overexpression of *per2* in WT neutrophils is sufficient to enhance neutrophil bactericidal activity and infection-responsive *hmgb1a* expression. (**A**) Expression of *per2* within neutrophils FACS-isolated from 52-hpf *Tg(lyz:DsRED2)* larvae under the LL and DD conditions (qRT-PCR, three experimental replicates per sample), normalized to the DD group. (**B** and **C**) Bacterial killing rates of (B) and ROS quantification within (C) *Sal*-GFP–laden neutrophils within *Tg(lyz:DsRED2)* larvae under conditions as shown in (A). (**D**) Expression of *hmgb1a* within neutrophils FACS-isolated from infected *Tg(lyz:DsRED2)* larvae under conditions as shown in (A) (qRT-PCR, three experimental replicates per sample), normalized to the DD group. (**E**) Kaplan-Meier graph of *Tg(lyz:DsRED2)* and *Tg(lyz:DsRED2);Tg(lyz:hmgb1a)* larvae infected under conditions as shown in (A), up to 5 dpi. (**F**) Bacterial killing rates of neutrophils within *Tg(lyz:DsRED2)* and *Tg(lyz:DsRED2);Tg(lyz:hmgb1a)* larvae under conditions as shown in (A). (**G**) Kaplan-Meier graph of *Tg(lyz:DsRED2)* and *Tg(lyz:DsRED2);Tg(lyz:per2)* larvae (infected at ZT4, LD condition), up to 5 dpi. (**H** and **I**) Bacterial killing rates of (H) and ROS quantification within (I) *Sal*-GFP–laden neutrophils within *Tg(lyz:DsRED2)* and *Tg(lyz:DsRED2);Tg(lyz:per2)* larvae (LD condition). (**J**) Expression of *hmgb1a* within neutrophils FACS-isolated from infected (infected at ZT4 LD condition) 2-dpf *Tg(lyz:DsRED2)* and *Tg(lyz:DsRED2);Tg(lyz:per2)* larvae (qRT-PCR, seven experimental replicates per sample), normalized to WT group. Data in (B), (F), and (H) were collected from three [(B) and (H)] or two or three (F) independent experiments per sample (*n* = 6 time-lapse movies per experiment), and data in (C), (E), (G), and (I) were collected from three independent experiments per sample. Error bars denote means ± SEM [(A), (D), and (J)] or means ± SD [(B), (C), (F), (H), and (I)]; **P* < 0.05, ***P* < 0.01, ****P* < 0.001, and *****P* < 0.0001; unpaired Student's *t* test [(A) to (D) and (H) to (J)], Gehan-Breslow-Wilcoxon test [(E) and (G)], or one-way ANOVA with Dunnett's multiple comparisons test (F).
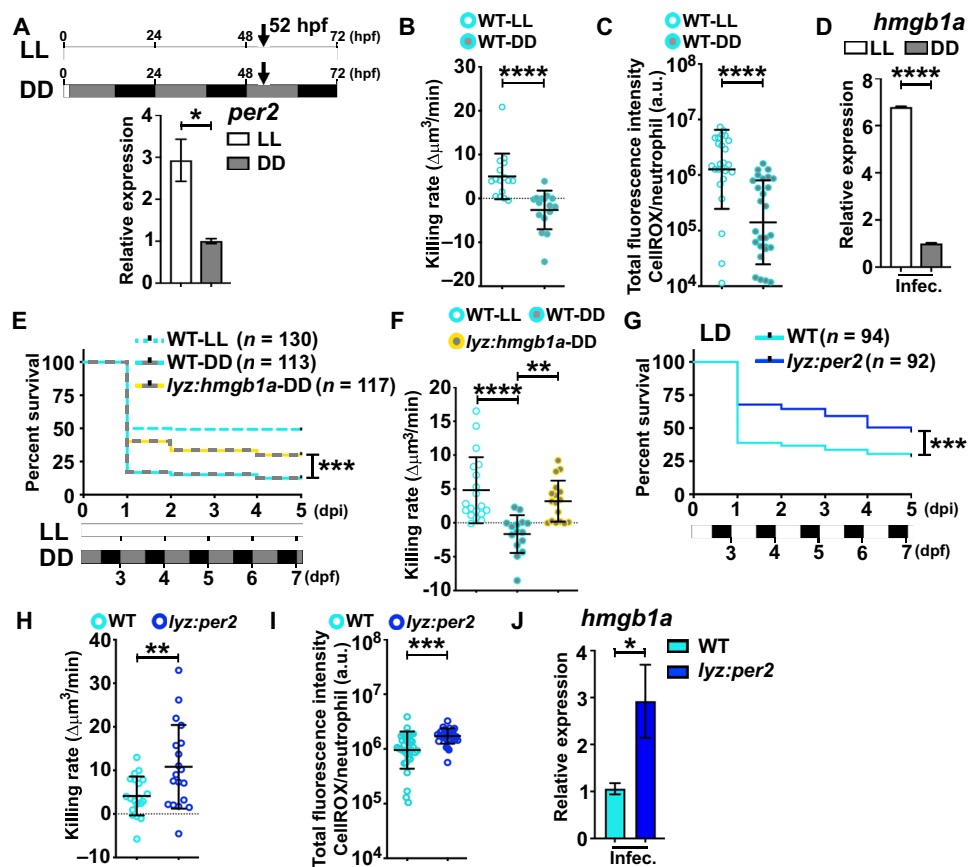
(fig. S7, B and C) in the DD condition increased survival and neutrophil killing rates toward levels seen in WT larvae infected under LL conditions (Fig. 5, E and F), independent of neutrophil abundance (fig. S7D).
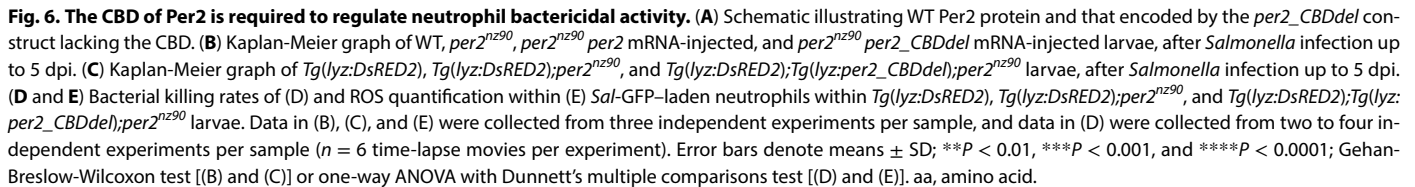
To evaluate whether Per2 was sufficient to enhance neutrophil function, we generated a *Tg(lyz:DsRED2);Tg(lyz:per2)* line (fig. S7E) that amplifies *per2* expression in neutrophils 27.7-fold within a WT background (fig. S7F). Despite having unaltered neutrophil numbers in whole larvae (fig. S7G), these larvae were protected from infection (18.9% increase in survival) (Fig. 5G), a phenotype accompanied by elevated neutrophil killing rates (Fig. 5H) and ROS production (1.8-fold increase in mean CellROX fluorescence intensity) (Fig. 5I). In addition, although SS levels of *hmgb1a* expression were unaltered in *per2*-overexpressing neutrophils (fig. S7H), infection-responsive expression increased 2.9-fold (Fig. 5J). Thus, light positively regulates *per2* expression in neutrophils and promotes neutrophil bactericidal activity and infection-responsive (but not SS) *hmgb1a* expression. Furthermore, elevating Per2 levels in neutrophils is sufficient to enhance these phenotypes.

Per2 and its interaction partner Cry1a have opposing roles in regulating neutrophil bactericidal activity

To investigate the requirement of Per2-Cry interaction for neutrophil bactericidal activity, we constructed a *per2* expression vector with an in-frame deletion removing the highly conserved C-terminal CRY-binding domain (CBD) spanning amino acid residues 1268 to 1382 (*per2_CBDdel*) (Fig. 6A and fig. S7I). Protein immunoblot of cells transfected with a His-tagged *per2_CBDdel* expression construct confirmed that *per2_CBDdel* can form a stable protein (fig. S7J). In contrast with WT *per2*, the overexpression of *per2_CBDdel* mRNA failed to rescue survival of infected *per2^{nz90}* larvae (Fig. 6B and fig. S7K). Next, we established the transgenic line *Tg(lyz:DsRED2); Tg(lyz:per2_CBDdel);per2^{nz90}* that drove *per2_CBDdel* expression within *per2^{nz90}* neutrophils (fig. S7, L to O). Overexpressing *per2_CBDdel* in *per2^{nz90}* neutrophils was also insufficient to rescue survival or elevate neutrophil bactericidal activity (Fig. 6, C to E, and fig. S7P). Because these results suggested that Per2 needs to interact with Cry to augment neutrophil bactericidal activity, we sought to examine bactericidal activity in Cry1a-deficient neutrophils.

We generated a *cry1a* mutant line (*cry1a^{nz91}*) with a premature stop codon within the photolyase-encoding domain (115 amino acids versus 619 amino acids for WT Cry1a) using an sgRNA targeting the first intron (fig. S8A). Neutrophils within *cry1a^{nz91}* larvae had a 3.6-fold reduction in *cry1a* expression (fig. S8B) and, similar to *per2^{nz90}* larvae, expression levels of selected clock genes demonstrated rhythmicity of expression comparable to that of WT larvae, with some changes to peak levels (fig. S8C). However, in contrast with *per2^{nz90}* larvae, those lacking Cry1a function were protected from infection in all lighting conditions (Fig. 7, A to D) and had significantly reduced bacterial loads (Fig. 7E). Overexpressing *cry1a* mRNA within

Fig. 6. The CBD of Per2 is required to regulate neutrophil bactericidal activity. (**A**) Schematic illustrating WT Per2 protein and that encoded by the *per2_CBDdel* construct lacking the CBD. (**B**) Kaplan-Meier graph of WT, *per2^nz90^*, *per2^nz90^ per2* mRNA-injected, and *per2^nz90^ per2_CBDdel* mRNA-injected larvae, after *Salmonella* infection up to 5 dpi. (**C**) Kaplan-Meier graph of *Tg(lyz:DsRED2)*, *Tg(lyz:DsRED2);per2^nz90^*, and *Tg(lyz:DsRED2);Tg(lyz:per2_CBDdel);per2^nz90^* larvae, after *Salmonella* infection up to 5 dpi. (**D** and **E**) Bacterial killing rates of (D) and ROS quantification within (E) *Sal*-GFP–laden neutrophils within *Tg(lyz:DsRED2)*, *Tg(lyz:DsRED2);per2^nz90^*, and *Tg(lyz:per2_CBDdel);per2^nz90^* larvae. Data in (B), (C), and (E) were collected from three independent experiments per sample, and data in (D) were collected from two to four independent experiments per sample (*n* = 6 time-lapse movies per experiment). Error bars denote means ± SD; **P < 0.01, ***P < 0.001, and ****P < 0.0001; Gehan-Breslow-Wilcoxon test [(B) and (C)] or one-way ANOVA with Dunnett's multiple comparisons test [(D) and (E)]. aa, amino acid.

*cry1a^nz91^* larvae rescued the survival phenotype (fig. S8, D and E). When assessing neutrophil and macrophage recruitment, *cry1a^nz91^* larvae exhibited a 1.4-fold increase in neutrophil abundance at the infection site at 3 hpi (when numbers peak in WT larvae). By contrast, macrophage numbers showed a modest increase at 1 hpi (fig. S8, F and G). Total numbers of neutrophils and macrophages in whole larvae remained unchanged (fig. S8, H and I). Last, although macrophage killing rates and ROS production were similar between *cry1a^nz91^* and WT cells (fig. S8, J and K), Cry1a-deficient neutrophils killed intracellular bacteria faster (Fig. 7F), produced more ROS (6.7-fold increase in mean CellROX fluorescence intensity) (Fig. 7G), and had a 2.7-fold increase in *hmgb1a* expression levels compared with WT neutrophils after infection (Fig. 7H). Similar to *per2*, *cry1a* expression levels were not affected by infection within either neutrophils or macrophages (fig. S8L). Measuring the relative abundance of *per2* and *cry1a* transcript levels within neutrophils and macrophages at SS revealed that, whereas *cry1a* is expressed at similar levels, *per2* expression was higher within neutrophils (fig. S8M).

To assess the combined impact of Per2 and Cry1a inactivation on neutrophil function, killing rates and infection-induced expression of *hmgb1a* were quantified within *Tg(lyz:mCherry):per2^nz90^;cry1a^nz91^* larvae. Double-mutant cells resembled *cry1a^nz91^* neutrophils, with elevated killing rates (Fig. 7I) and infection-responsive *hmgb1a* expression (Fig. 7J).

Thus, Per2 requires its Cry binding domain to regulate neutrophil bactericidal activity. Furthermore, Cry1a and Per2 have opposing roles within neutrophils, with Cry1a suppressing and Per2 enhancing bactericidal activity. Given that *cry1a^nz91^* neutrophils phenocopy those overexpressing *per2* and that the *cry1a^nz91^* phenotype dominates within *per2^nz90^;cry1a^nz91^* neutrophils, our results imply that Per2 interacts with Cry1a when promoting infection-responsive *hmgb1a* expression.

hmgb1a contains an infection-responsive and light-regulated CRE containing BMAL1 and NF-κB motifs

Our observations revealed *hmgb1a* as a CCG within neutrophils where light primes infection-responsive expression. Circadian-gated expression of immune response genes could be regulated through rhythmic binding of CLOCK:BMAL1 within CREs that primes NF-κB–driven transcription (fig. S9A) (*23*). We therefore explored the genomic sequence upstream of *hmgb1a* for any conserved CREs containing CLOCK, BMAL1, or NF-κB binding motifs.

Alignment of zebrafish *hmgb1a* (inclusive of 11 kb of upstream sequence) with orthologs from other teleosts, *Xenopus*, chicken, and mammals uncovered four highly conserved noncoding regions, denoted as CNS1–4 (Fig. 8A and fig. S9B). Inspection of these regions for CLOCK, BMAL1, and NF-κB binding motifs revealed that only CNS4 had CLOCK and/or BMAL1 motifs across all examined species, except medaka (table S1). Furthermore, CNS4 contained putative binding sites for NF-κB in all species, excluding stickleback and *Xenopus* (table S1). Using the DANIO-CODE track hub browser (*50*), we found that the 345-bp sequence of zebrafish CNS4 overlapped with a consensus promoter region for *hmgb1a* (fig. S9B). To investigate whether zebrafish Bmal1a could physically interact with CNS4, we constructed a *bmal1a-His* expression construct (Fig. 8B) and confirmed its expression by protein immunoblot (fig. S9C). We then performed chromatin immunoprecipitation (ChIP)–qPCR on *bmal1a-His* mRNA- and PBS-injected embryos using primers specific to the putative BMAL1 site within CNS4 (Fig. 8C). This analysis showed that exogenously supplied Bmal1a
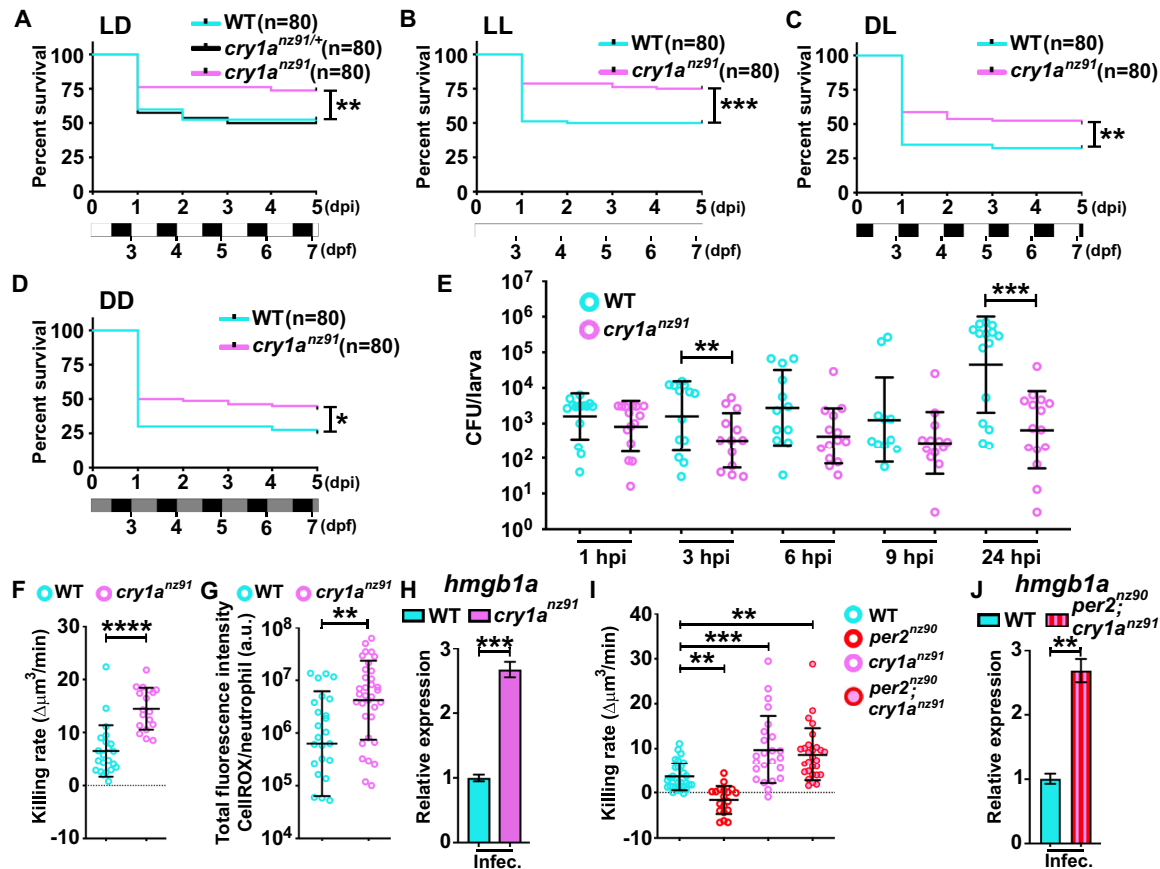
Fig. 7. Infected Cry1a-deficient larvae have enhanced survival and bacterial clearance, and their neutrophils have increased bactericidal activity and *hmgb1a* expression. (**A** to **D**) Kaplan-Meier graphs of WT, *cry1a^{nz91/+}* [(A) only], and *cry1a^{nz91}* larvae after *Salmonella* infection under LD (A), LL (B), reversed DL (C), and DD (D) conditions. (**E**) Bacterial burdens within WT and *cry1a^{nz91}* larvae at 1, 3, 6, 9, and 24 hpi with *Sal*-GFP (LD condition). (**F** and **G**) Bacterial killing rates of (F) and ROS quantification within (G) *Sal*-GFP–laden neutrophils within *Tg(lyz:DsRED2)* and *Tg(lyz:DsRED2);cry1a^{nz91}* larvae (LD condition). (**H**) Expression of *hmgb1a* within neutrophils FACS-isolated from infected (infected at ZT4 LD condition) 2-dpf *Tg(lyz:DsRED2)* and *Tg(lyz:DsRED2);cry1a^{nz91}* larvae (qRT-PCR, three experimental replicates per sample), normalized to the WT group. (**I**) Bacterial killing rates of WT, *per2^{nz90}*, *cry1a^{nz91}* and *per2^{nz90};cry1a^{nz91}* neutrophils within *Tg(lyz:DsRED2)*, *Tg(lyz:DsRED2);per2^{nz90}*, *Tg(lyz:DsR ED2);cry1^{nz91}*, and *Tg(lyz:mCherry);per2^{nz90};cry1a^{nz91}* larvae (LD condition). (**J**) Expression of *hmgb1a* within neutrophils FACS-isolated from infected (infected at ZT4 LD condition) 2-dpf *Tg(lyz:DsRED2)* and *Tg(lyz:mCherry);per2^{nz90};cry1a^{nz91}* larvae (qRT-PCR, three experimental replicates per sample), normalized to WT group. Data in (A) to (D) and (G) were collected from three independent experiments per sample, and data in (F) and (I) were collected from three (F) and six to eight (I) independent experiments per sample (*n* = 6 time-lapse movies per experiment). Error bars denote means ± SD [(E) to (G) and (I)] or means ± SEM [(H) and (J)]; *$P < 0.05$, **$P < 0.01$, ***$P < 0.001$, and ****$P < 0.0001$; Gehan-Breslow-Wilcoxon test [(A) to (D), unpaired Student's *t* test [(E) to (H) and (J)], or one-way ANOVA with Dunnett's multiple comparisons test (I).

can bind to CNS4 (Fig. 8D). To assess the transcriptional activity of this conserved putative CRE, we cloned CNS4 together with 500 bp of flanking genomic sequence into a Tol2-based *E1b:GFP* reporter construct (containing the *E1b* minimal promoter) to generate the stable line *Tg(hmgb1aCNS4-E1b:GFP)* (Fig. 8E). Similar to endogenous *hmgb1a* expression, as shown here (fig. S9, F and G) and previously (*51*), GFP expression within *Tg(hmgb1aCNS4-E1b:GFP)* larvae was largely ubiquitous, with notable enrichment in the developing brain, fin placode, neuromasts, and neural tube at 2 dpf (Fig. 8F and fig. S9, D and E). To investigate the impact of light and infection on the transcriptional activity of CNS4, *GFP* expression was quantified from *Tg(hmgb1aCNS4-E1b:GFP)* larvae after infection with nonfluorescent *Salmonella* (or control PBS injection) at 52 hpf under both LL and DD conditions (fig. S9H). This analysis revealed a 4.6-fold increase in *GFP* expression after infection that was restricted to the light condition (fig. S9I). Thus, CNS4 operates

as a CRE of *hgmb1a* to promote infection-responsive expression during the light phase.

The *hmgb1a* BMAL1 motif controls infection-responsive light-gated transcription of *hmgb1a* during the light phase to regulate neutrophil bactericidal activity

We next investigated the role of the BMAL1 motif in CNS4 in the light-induced regulation of infection-driven transgene expression in *Tg(hmgb1aCNS4-E1b:GFP)* larvae. After evaluating two CRISPR sgRNAs (CNS4 sgRNAs1 and 2) to target the endogenous CNS4 BMAL1 motif in WT larvae (fig. S10A), we assessed which was most effective at editing the motif within the *hmgb1aCNS4-E1b:GFP* transgene while leaving the neighboring NF-κB motif intact. Although both sgRNAs achieved efficient editing at their target sites (fig. S10, B to F), analysis of edits restricted to the BMAL1 and NF-κB motifs, inclusive of 5-bp proximal and distal flanking regions that

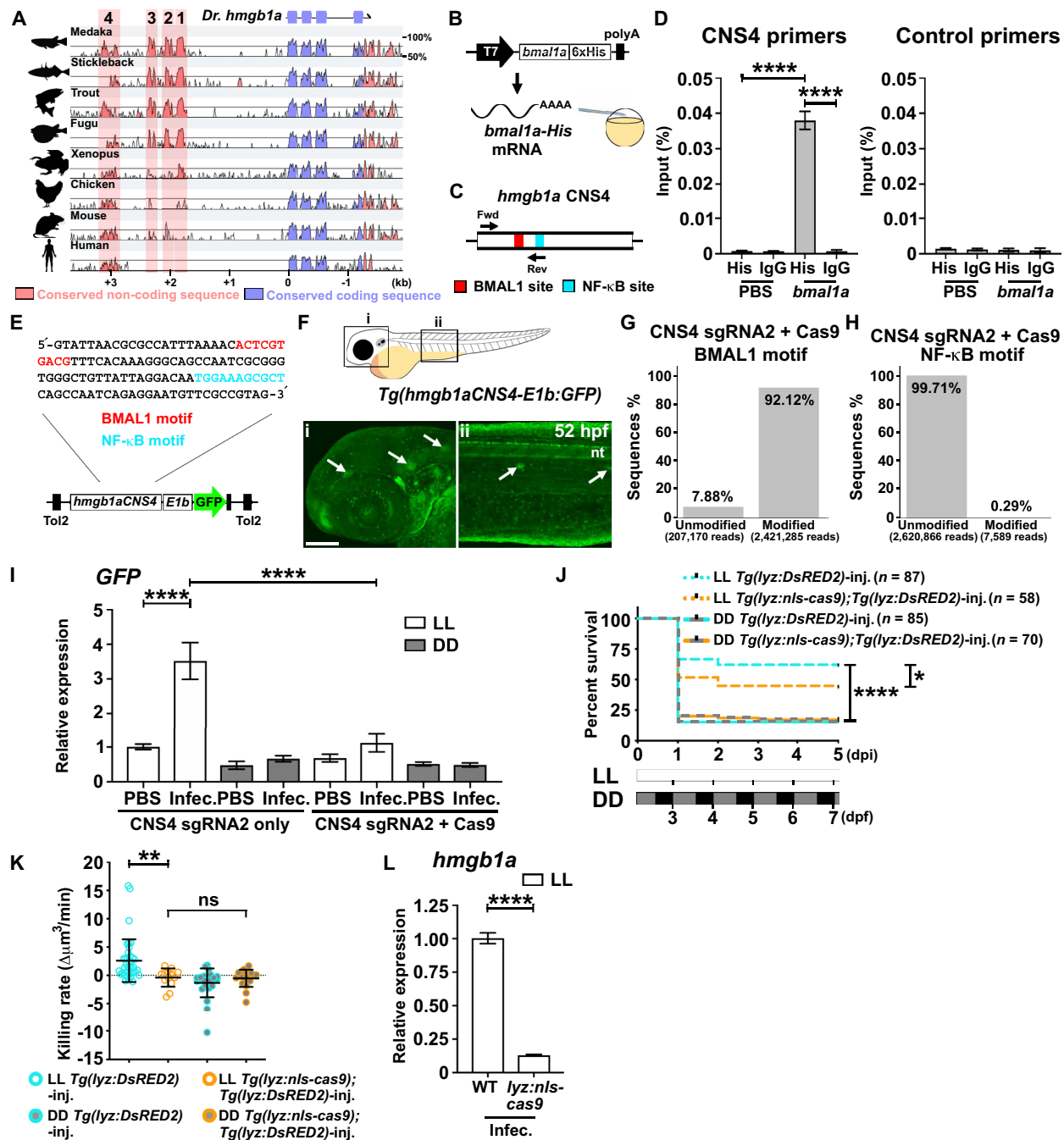**Fig. 8. A conserved CRE of *hmgb1a* contains BMAL1 and NF-κB binding motifs and regulates light-dependent infection-responsive transcription and neutrophil bactericidal activity.** (**A**) Sequence alignment of zebrafish (*Danio rerio*) *hmgb1a* showing four conserved noncoding sequence (CNS) regions in orange. Purple marks coding regions. (**B**) Schematic of *bmal1a-His* expression construct. (**C**) Schematic of ChIP-qPCR primers for *hmgb1a* CNS4. (**D**) ChIP-qPCR for exogenous Bmal1a binding to *hmgb1a* CNS4 within PBS- or *bmal1a-His* mRNA-injected embryos using anti-His Tag and IgG isotype control antibodies, compared with control primers (*n* = 100 larvae per sample in experimental triplicate). (**E**) Schematic of *hmgb1aCNS4-E1b:GFP* construct. (**F**) Live imaging of *Tg(hmgb1aCNS4-E1b:GFP)* larvae at 52 hpf (ZT4 LD conditions) highlighting expression within neuromasts (arrows) and neural tube (nt). Scale bar, 100 μm. (**G** and **H**) Frequencies of unmodified and modified BMAL1 (G) and NF-κB (H) motifs from 2-dpf *Tg(hmgb1aCNS4-E1b:GFP)* larvae injected with CNS4 sgRNA2 + Cas9. (**I**) *GFP* expression within CNS4 sgRNA2 + Cas9– or CNS4 sgRNA2-only–injected *Tg(hmgb1aCNS4-E1b:GFP)* larvae under LL and DD conditions, 3 hpi with PBS or nonfluorescent *Salmonella* (qRT-PCR, *n* = 20 larvae per sample in experimental triplicate), normalized to LL PBS CNS4 sgRNA2–only group. (**J**) Kaplan-Meier graph of CNS4 sgRNA2–injected *Tg(lyz:DsRED2)* and *Tg(lyz:nls-cas9);Tg(lyz:DsRED2)* larvae under LL and DD conditions, up to 5 dpi. (**K**) Neutrophil bacterial killing rates within CNS4 sgRNA2–injected *Tg(lyz:DsRED2)* and *Tg(lyz:nls-cas9);Tg(lyz:DsRED2)* larvae under LL and DD conditions. (**L**) *hmgb1a* expression in neutrophils FACS-isolated from infected CNS4 sgRNA2–injected *Tg(lyz:DsRED2)* and *Tg(lyz:nls-cas9);Tg(lyz:DsRED2)* larvae under LL conditions (qRT-PCR, three experimental replicates per sample), normalized to the WT group. Data in (J) were collected from three independent experiments per sample, and data in (K) were collected from three to five independent experiments per sample (*n* = 6 time-lapse movies per experiment). Error bars denote means ± SEM [(D), (I), and (L)] or means ± SD (K); *P < 0.05, **P < 0.01, and ****P < 0.0001; one-way ANOVA with Dunnett's multiple comparisons test [(D), (I), and (K)], Gehan-Breslow-Wilcoxon test (J), or unpaired Student's t test (L).

contribute to binding specificity (*52*) (fig. S10G), revealed that CNS4 sgRNA2 had the highest editing efficiency at the BMAL1 motif (92.12%) and the lowest at the NF-κB site (0.29%) (Fig. 8, G and H, and fig. S10, H and I). Subsequent LL and DD infection experiments revealed that mutagenesis of the BMAL1 motif within *hmgb1aCNS4-E1b:GFP* using CNS4 sgRNA2 significantly reduced infection-responsive transgene expression under the LL condition (Fig. 8I and fig. S10J).

To assess the importance of the endogenous *hmgb1a* BMAL1 motif in neutrophils, we targeted it using CNS4 sgRNA2 and our neutrophil-editing *Tg(lyz:nls-cas9);Tg(lyz;DsRED2)* line (fig. S10K). This approach successfully targeted editing to neutrophils (fig. S10, L to O) and achieved 70% editing at the BMAL1 motif while preserving the NF-κB motif (fig. S10, P to R). Neutrophil-specific mutagenesis of the BMAL1 motif diminished the positive effect of light on postinfection survival (17.8% decrease in survival) (Fig. 8J) and removed the priming effect of light on neutrophil bactericidal activity (Fig. 8K). In addition, editing the BMAL1 motif in neutrophils resulted in a 7.7-fold decrease in infection-responsive *hmgb1a* expression in the light condition (Fig. 8L). Nanopore sequencing of genomic DNA isolated from WT and CNS4 sgRNA2 + Cas9-injected larvae revealed no evidence of off-target editing at two characterized E-box/BMAL1 binding sites upstream of the genes *aanat1* and *aanat2* (fig. S10S) (*53*, *54*).

These results suggest CNS4 functions as a CRE that synchronizes infection-responsive expression of *hmgb1a* in neutrophils to the light phase, thereby enhancing bactericidal activity. Moreover, the BMAL1 motif within CNS4 plays an essential role in facilitating the light-primed infection-responsive transcriptional activity of this conserved CRE.

DISCUSSION

Host protection against bacterial pathogens, including *Salmonella*, *Streptococcus pneumoniae*, and *Chlamydia muridarum*, is greatest when infections occur during an animal's active phase (*9*, *35*, *55*, *56*). This has contributed to the view that the circadian system likely boosts antibacterial immunity as animals transition to activity and the risk of infection increases (*2*, *3*). Neutrophil abundance in the circulation and tissues is known to oscillate in a circadian manner, with peak numbers in tissues coinciding with the active phase (*25*, *26*). This circadian-gated egress of neutrophils from the circulation into tissues is dependent on BMAL1-driven expression of the chemokine *Cxcl2* (*27*). Here, we show that neutrophils provide a critical component of the circadian-gated host response to infection by demonstrating that they use their circadian clock machinery to transcriptionally amplify bactericidal activity during the active phase.

A primary bactericidal weapon in the neutrophil arsenal is the production of ROS by the NOX2 oxidase (*57*–*59*). After phagocytosis of bacteria, neutrophils assemble the NOX2 complex that consumes O_2 to generate highly reactive ROS (including O_2^-, H_2O_2, and HOCl) to kill intraphagosomal bacteria. Through live imaging of this process, we show that Per2-deficient neutrophils generate significantly less NOX–generated ROS that, at least in part, explains their inability to kill intracellular bacteria efficiently. Transcriptomic analysis of *per2^{nz90}* neutrophils uncovered *hmgb1a* as a Per2-regulated gene that amplifies neutrophil bactericidal ROS production during the light phase. In response to infection and tissue damage, HMGB1

can be actively secreted (primarily from macrophages) or passively released from damaged cells where it functions as a DAMP to mediate immune responses (*45*, *60*, *61*). Immune cells sense extracellular HMGB1 through several receptors, including receptor for advanced glycation end products (RAGE), Toll-like receptor 2 (TLR2), and TLR4 (*45*, *60*). HMGB1 is a potent chemoattractant for neutrophils (*62*, *63*) and can stimulate activation of the NOX complex (and ROS production) in mouse neutrophils through TLR4 (*64*). By showing that elevated levels of *per2* in neutrophils align with the light phase and contribute to increased infection-responsive expression of *hmgb1a*, we describe a function for neutrophil-derived Hmgb1a. We speculate that this source of Hmgb1a acts on neutrophils in an autocrine/paracrine manner to stimulate elevated ROS production. Enhanced *hmgb1a* expression has recently been described within neutrophils that contribute to zebrafish heart regeneration (*65*).

An interesting observation from our study was the absence of a bactericidal phenotype within Per2- and Cry1a-deficient macrophages, at least when examining killing rates and ROS production at 3 hpi. In addition, we showed that macrophages do not up-regulate *hmgb1a* expression after infection when assessed at 3 hpi. When looking at the relative abundance of *per2* and *cry1a* transcripts at ZT4 (the time point when infections were delivered), we saw that neutrophils express higher levels of *per2* when compared with macrophages, suggesting that the clock machinery likely differs between these cell types and that neutrophils may be inherently more sensitive to Per2 deficiency. Despite this, we anticipate that other effector functions (for example, cytokine expression) are likely affected in *per2^{nz90}* and *cry1a^{nz91}* macrophages. Furthermore, examining macrophages at later time points postinfection (beyond the 3 hours described here) may reveal additional defects. Neutrophil-restricted expression of *per2* and *hmgb1a* did not completely rescue survival of infected *per2^{nz90}* larvae, strongly suggesting other host-protective functions for Per2, independent of the neutrophil-specific role we describe here. The survival of larvae overexpressing *hmgb1a* within neutrophils and infected in the DD condition was also not as high as in WT larvae infected in the LL condition. This result implies that light promotes additional antibacterial responses other than the neutrophil-Per2-Hmgb1a mechanism we report here. Last, neutrophil-targeted expression of *per2* did not rescue the neutrophil recruitment defect observed within infected *per2^{nz90}* larvae, suggesting that Per2 functions within another cell type to promote neutrophil migration.

This work reveals a positive role for Per2 in driving infection-responsive *hmgb1a* expression in neutrophils, aligning with other studies showing that PER2 can positively regulate gene expression. For example, PER2 can bind CRY1 and form an "inactive repressor" complex that functions early in the circadian cycle as a time delay, prolonging the transcriptional activity of the CLOCK:BMAL1 heterodimer (*6*). Studies have also shown that PER2 can interfere with the binding of CRY to the CLOCK:BMAL1:DNA complex and that CRY alone is the primary repressor of CLOCK:BMAL1-driven transcription (*7*, *8*). We show that neutrophil-specific overexpression of *per2* lacking the CBD did not rescue bactericidal defects of *per2^{nz90}* neutrophils. In addition, *cry1a^{nz91}* neutrophils have an opposite bactericidal phenotype to those lacking Per2, with enhanced bactericidal activity and infection-induced *hmgb1a* expression, phenotypes that dominate within double-mutant *per2^{nz90}*;*cry1a^{nz91}* larvae. These observations lead us to hypothesize that Per2 supports *hmgb1a* expression by forming an inactive repressor complex with Cry1a.

Sufficiently high levels of Per2 in neutrophils during the light phase prevent Cry1a from suppressing CLOCK:BMAL1-driven *hmgb1a* expression, whereas its absence in Per2-deficient neutrophils allows Cry1a to freely repress CLOCK:BMAL1. The fact that *cry1a*[nz91] larvae are protected from infections in all lighting conditions also suggests that Cry1a contributes to the host response to infection during the dark phase when transcript levels are at their lowest. In mouse liver nuclei, CRY1 and PER2 protein levels peak at different circadian times, with PER2 abundance restricted to a tighter temporal window than those of CRY1 (*7*). Without available antibodies against zebrafish Per2 and Cry1a, examining nuclear abundance within neutrophil nuclei was beyond the scope of this investigation.

Our results have shown that infecting larvae under the LL condition leads to enhanced survival, partly because of elevated infection-induced *hmgb1a* expression and neutrophil bactericidal activity. Given that constant light would result in dysregulated circadian rhythmicity, these results suggest that the circadian-gated neutrophil bactericidal activity we describe here is likely regulated by light rather than by a true circadian clock mechanism that would maintain oscillations in gene expression in the absence of external cues. Considering the short life span of neutrophils [generally accepted to be less than one complete circadian cycle (*66*)], regulating circadian-gated activity through oscillations in gene expression within a given neutrophil seems even less intuitive. A BMAL1-dependent cellular timer has been proposed to operate in mouse neutrophils to control the process of neutrophil "aging" and the circadian-gated egress of "aged" neutrophils from the circulation into tissues (*27*). The authors of this study similarly suggest, given their short life span, that the neutrophil clockwork does not function as a true circadian clock but instead as a cellular timer within individual cells to help orchestrate diurnal changes at a population level (*27*).

The CLOCK:BMAL1 heterodimer has been proposed to rhythmically bind to CREs of CCGs and co-regulate expression with tissue-specific and inducible transcription factors, including NF-κB. This interaction is believed to drive tissue-specific rhythms in CCG expression under certain conditions, such as during inflammatory responses (*23, 67–70*). We identified a conserved CRE (CNS4) for *hmgb1a* that has a BMAL1 binding motif that can bind exogenously supplied Bmal1a and an NF-κB binding site. Genetic disruption of the BMAL1 binding site in CNS4 confirmed its crucial role in facilitating light-induced infection-responsive *hmgb1a* expression in neutrophils and in regulating increased neutrophil bactericidal activity under LL conditions. We speculate that during the light phase, when Per2 levels are sufficiently elevated to counteract Cry1a-mediated repression of CLOCK:BMAL1, the CLOCK:BMAL1 heterodimer primes NF-κB accessibility, most likely by chromatin modification (*18–22, 68*), to facilitate amplified *hmgb1a* expression in neutrophils during infection (fig. S11). This model offers a rationale for the priming effect of light on infection-driven *hmgb1a* expression in neutrophils. It also explains the increase in *hmgb1a* expression within *per2*-overexpressing neutrophils upon infection only and the opposing roles of Per2 and Cry1a in regulating *hmgb1a* expression and neutrophil bactericidal activity. CNS4 was also conserved upstream of mouse and human *HMGB1*, suggesting that our observations may translate to mammalian neutrophils. Major limitations to studying human neutrophils in vitro include their limited life span, inability to proliferate, and resistance to genetic manipulation, whereas cell lines lack the antimicrobial capacity of isolated cells (*71, 72*). In addition, live imaging of neutrophil behavior at the single-cell level in mice remains technically challenging. Future efforts to overcome these obstacles will provide opportunities to live-image mammalian neutrophils in vivo and explore whether they similarly use circadian clock components to regulate intracellular antibacterial activity.

Limitations of our study include the inability to examine Per2, Cry1a, or Bmal1a protein levels within neutrophils because of a lack of suitable antibodies. Investigating the nuclear occupancy of Per2 and Cry1a within neutrophils throughout a circadian cycle and comparing their relative abundance may help explain their opposing contributions to infection-responsive *hmgb1a* expression and help resolve why *cry1a*[nz91] larvae are protected from infection during the dark phase when transcript levels of *cry1a* are lowest. Furthermore, zebrafish-specific or cross-reacting antibodies would also enable global analysis of Per2, Cry1a, and Bmal1a occupancy within neutrophils through ChIP-seq, a technique recently demonstrated using neutrophils FACS-isolated from larval zebrafish (*73*). In addition, although we show that neutrophils express higher levels of *per2* under constant light conditions when compared with constant dark, technical limitations associated with FACS-isolating neutrophils over a complete circadian cycle precluded investigating whether expression levels oscillate similarly to those observed in whole larvae. Last, the precise mechanism through which *hmgb1a* expression in neutrophils contributes to ROS production and bactericidal activity remains unknown.

In summary, by using the live imaging of transparent larval zebrafish, we show that neutrophil bactericidal activity is circadian-gated, is transcriptionally controlled by the core clock components Per2 and Cry1a, and functions to boost host protection during the active phase. Our work provides fundamental mechanistic insights into the transcriptional regulation of CCGs in immune cells, describes an additional function for the evolutionarily conserved protein HMGB1, helps explain time-of-day variations in host antibacterial defense, and raises the possibility of targeting the neutrophil clockwork to better manage bacterial infections.

MATERIALS AND METHODS
Study design
This study was designed to examine how *per2* contributes to the host response to infection. We generated *per2* mutant zebrafish and characterized the larval response to *Salmonella* infection under different lighting conditions. Live imaging of infected Per2-deficient animals revealed that neutrophils generated less bactericidal ROS and killed intracellular bacteria less efficiently. We used cell transplantation experiments and generated a neutrophil-specific *per2* rescue line to determine whether Per2 was cell-autonomously required for neutrophil bactericidal activity. Bulk RNA-seq of neutrophils uncovered *hmgb1a* as a Per2-dependent infection-responsive gene and that neutrophil-specific mutation of *hmgb1a* reduced bactericidal activity. A transgenic rescue line overexpressing *hmgb1a* within neutrophils was generated that restored neutrophil bactericidal activity in Per2-deficient larvae. A transgenic line overexpressing a truncated *per2* lacking the Cry binding domain revealed that this domain was necessary for the positive impact of Per2 on neutrophil bactericidal activity. For this study, we also generated *cry1a* mutant zebrafish that were protected from infection with enhanced neutrophil bactericidal activity and infection-responsive *hmgb1a* expression, phenotypes that were dominant in *per2;cry1a* double mutant larvae. Last, multispecies genomic alignment uncovered a conserved CRE

that can bind Bmal1a and restrict infection-responsive expression of *hmgb1a* to the light phase, thereby enhancing neutrophil bactericidal activity. Larvae were randomly assigned to experimental groups to which researchers were not blinded. The number of experimental replicates is indicated in each figure legend. All data were included.

Zebrafish and lighting conditions
All zebrafish research was conducted with the approval of the University of Auckland Animal Ethics Committee (approval numbers AEC001911 and AEC22563). Adult zebrafish (*Danio rerio*) were housed in the University of Auckland's Faculty of Medical and Health Sciences Zebrafish Facility on a 14 hour–10 hour LD cycle (350 lux versus <1 lux). Larval zebrafish were generated by natural spawning and raised at 28°C in standard E3 medium (0.33 mM $CaCl_2$, 0.33 mM $MgSO_4$, 0.17 mM KCl, and 5 mM NaCl) supplemented with 0.003% phenyl-thiourea (PTU) to inhibit pigmentation and when appropriate anes-thetized by supplementing E3 with 4% (v/v) tricaine. For LD and LL treatments, embryos were harvested and raised under 14- to 10-hour LD (400 lux versus <1 lux) or constant light (LL, 400 lux) conditions within environmental incubators (maintained at 28°C). For reversed DL and DD conditions, embryos were harvested within 1 hour of spawning and similarly raised in environmental chambers under 10- to 14-hour DL or DD conditions. WT AB zebrafish were obtained from the Zebrafish International Resource Centre (ZIRC). The neutrophil-specific *Tg(lyz:DsRED2)*[nz50] (*31*) and macrophage-marking *Tg(mpeg1:EGFP)*[gl22] and *Tg(mpeg1:Gal4FF)*[gl25];*Tg(UAS-E1b:nfsB-mCherry)*[c264] [herein referred to as *Tg(mpeg1:mCherry)*] reporter lines were used (*29*, *74*).

Generation of *per2* and *cry1a* mutant lines
Target sites for *per2*-targeting sgRNAs 1 and 2 were designed us-ing CHOPCHOP (*75*). For sgRNA1, oligonucleotides (see table S2 for oligonucleotide sequences) were annealed and cloned into the T7cas9sgRNA2 vector (*76*). After cloning and sequencing verifica-tion, the vector was linearized with Bam HI, and sgRNA1 was tran-scribed using the MEGAshortscript T7 kit (Ambion) according to the manufacturer's protocol. For sgRNA2, the partially overlapping oligonucleotides containing the sgRNA2 target region, SP6 promoter, and gRNA scaffold sequence were annealed (see table S2 for oligo-nucleotide sequences). T4 DNA polymerase (New England Biolabs) was used to fill in 5′ overhangs, followed by sgRNA2 transcription using the SP6 MEGAscript kit (Amion), as per the manufacturer's protocol. Cas9 mRNA [produced using the pT3TS-nls-zCas9-nls plasmid (*76*) and the mMESSAGE mMACHINE T3 transcription kit (Ambion)] and sgRNA 1 and 2 were injected into the cytoplasm of one-cell–stage WT embryos. The −1774-bp deletion mutation gen-erated here in the *per2* gene was given the allele designation of *per2*[nz90]. The *cry1a*-targeting sgRNA was designed using CHOPCHOP, and partially overlapping oligonucleotides containing the target region, SP6 promoter, and gRNA scaffold sequence were annealed (see table S2 for oligonucleotide sequences) and transcribed as above. The −6/+5 bp mutation generated here in the *cry1a* gene was given the allele desig-nation of *cry1a*[nz91].

Generation of transgenic lines
To create the *lyz:per2* transgenic construct, the full-length open read-ing frame (ORF) of *per2* was amplified using Platinum SuperFi II DNA polymerase (Life Technologies, Thermo Fisher Scientific) (see table S2 for oligonucleotide sequences. The resulting amplicon was cloned into pENTR/D-TOPO (Life Technologies, Thermo Fisher Scientific) to generate the *per2*/pENTR/D-TOPO middle entry vector. After sequence verification, *per2*/pENTR/D-TOPO was gateway-cloned into pDestTol2CG2 with p5E-lyz, p3E-polyA using the Tol2 kit (*77*). The *lyz:per2* construct was injected into one-cell–stage *Tg(lyz:DsRED2)*[nz50] and *Tg(lyz:DsRED2)*[nz50];*per2*[nz90] embryos, along with Tol2 transposase RNA, to create the stable lines *Tg(lyz:DsRED2)*[nz50];*Tg(lyz:per2)*[nz92] [herein referred to as *Tg(lyz:DsRED2);Tg(lyz:per2)*] and *Tg(lyz:DsRED2)*[nz50];*Tg(lyz:per2)*[nz93];*per2*[nz90] [herein referred to as *Tg(lyz:DsRED2);Tg(lyz:per2);per2*[nz90]], respectively. The same strategy was also used to generate the stable lines *Tg(lyz:DsRED2)*[nz50];*Tg(lyz:hmgb1a)*[nz97] [herein referred to as *Tg(lyz:DsRED2);Tg(lyz:hmgb1a)*] and *Tg(lyz:DsRED2)*[nz50];*Tg(lyz:hmgb1a)*[nz98];*per2*[nz90] [herein referred to as *Tg(lyz:DsRED2);Tg(lyz:hmgb1a);per2*[nz90]]. Similar injection of *lyz:per2_CBDdel* into *Tg(lyz:DsRED2)*[nz50];*per2*[nz90] generated the *Tg(lyz:DsRED2)*[nz50];*Tg(lyz:per2_CBDdel)*[nz94];*per2*[nz90] line [herein referred to as *Tg(lyz:DsRED2);Tg(lyz:per2_CBDdel);per2*[nz90]]. To create the *hmgb1aCNS4-E1b:GFP* transgene, ±500 bp of genomic sequence flanking CNS4 was amplified from genomic DNA using Platinum SuperFi II DNA polymerase (Life Technologies, Thermo Fisher Sci-entific) and forward and reverse primers with incorporated Sfi I and Bgl II restriction sites (see table S2 for oligonucleotide sequences). The resulting amplicon was cloned into the pCRBlunt II-TOPO vector (Life Technologies, Thermo Fisher Scientific), sequence-verified, and subcloned into Sfi I/Bgl II–linearized E1b-GFP-Tol2 (a Tol2-based enhancer screening vector containing the E1b minimal promoter up-stream of GFP) (*78*) to generate the *hmgb1aCNS4-E1b:GFP* trans-genesis construct. Coinjection of *hmgb1aCNS4-E1b:GFP* and Tol2 transposase RNA into one-cell–stage WT embryos created the stable line *Tg(hmgb1aCNS4-E1b:GFP)*[nz95]. The *Tg(lyz:nls-cas9)*[nz96];*Tg(lyz:DsRED2)*[nz50] reporter line [herein referred to as *Tg(lyz:nls-cas9);Tg(lyz:DsRED2)*] was created in house from a plasmid gifted for use in this study (*47*). To create the *Tg(lyz:mCherry)*[nz99];*per2*[nz90];*cry1a*[nz91] stable line [herein referred to as *Tg(lyz:mCherry);per2*[nz90];*cry1a*[nz91]], a *lyz:mCherry* construct (created using p5E-lyz with pDestTol2pA, pME-mCherry, and p3E-polyA from the Tol2 kit) was injected into one-cell–stage *per2*[nz90];*cry1a*[nz91] embryos.

Infections and survival analysis
Infections and survival analyses were performed as previously de-scribed (*40*). In brief, larvae were anaesthetized in tricaine and ar-rayed in 3% methyl cellulose (in E3 medium) and infected with 1000 CFU of GFP-expressing *S. enterica* serovar Typhimurium [*Sal*-GFP, strain SM022 (*79*)] or nonfluorescent *Salmonella* (strain SL1344) by hindbrain microinjection at 52 hpf (ZT4 and ZT16 for the LD and DL conditions, respectively). *Salmonella* were inocu-lated into 4 ml of lysogeny broth (LB) and cultured overnight at 27°C followed by a 10-fold dilution into 16 ml of LB and 20 ml of Dulbecco's modified Eagle's medium (DMEM; Gibco) and incuba-tion at 37°C for 45 min. The CFU of the culture was estimated on a spectrophotometer (optical density at 600 nm). For infections in the dark phase (DD and DL infections), larvae were arrayed and infected in small groups under dim light (1 to 2 lux) to minimize light exposure (~10 min of dim light exposure per group). Infected larvae (approximately 20 to 30) were placed into 100-mm petri dishes and monitored daily for death (cardiac arrest). Dead larvae were removed, and any displaying excessive *Sal*-GFP dissemination

(as detected by fluorescence microscopy) were transferred to a separate petri dish to prevent bacterial spread through the E3 medium in the event of death and larvae dissociation between monitoring periods. Larvae were monitored for death during the light period for the LD, LL, and DL conditions and under dim light (1 to 2 lux) for the DD condition. For all survival analyses, infections were 1000 CFU at 52 hpf (ZT4 and ZT16 for LD and DL conditions, respectively) unless otherwise stated.

RNA isolation, cDNA synthesis, RT-PCR, and qRT-PCR
For RT-PCR and qRT-PCR expression analysis for whole larvae, RNA was extracted from whole larvae (approximately 30 larvae) at 4-hour intervals starting from ZT0 (48 or 120 hpf) to ZT4 (76 or 148 hpf) under LD for qRT-PCR using TRIzol (Life Technologies, Thermo Fisher Scientific), as per the manufacturer's recommendations. RNA from FACS-isolated cells was isolated using the RNeasy micro kit (QIAGEN), as per the manufacturer's protocol. When detecting mutant *per2* transcript and checking *hmgb1a* MO specificity, cDNA was synthesized using SuperScript III reverse transcriptase (Life Technologies, Thermo Fisher Scientific). For all other applications, cDNA was synthesized from RNA using iScript cDNA synthesis kit (Bio-Rad). qRT-PCR was performed in, at least, technical duplicate using a QuantStudio 6K Flex real-time PCR system (Life Technologies, Thermo Fisher Scientific) using PerfeCTa SYBR Green FastMix (Quantabio). Expression levels were normalized to *ef1a* and calculated using the $\Delta\Delta$Ct method (see table S2 for oligonucleotide sequences). To assess *hmgb1a* MO–induced splicing defects and *lyz:per2_CBDdel* expression, RT-PCR was performed (see table S2 for oligonucleotide sequences).

Behavioral recording
Activity recordings were collected using a Zebrabox (ViewPoint Life Sciences) behavior analysis system with ZebraLab tracking software. Recordings of the total distance moved (millimeter) were collected using the quantification mode with the following parameters: integration period, 10 min; detection threshold, 30; inactivity/small movement, <1 mm/s; small/large threshold, ≥1 mm/s. A custom-built program using the Python package Matplotlib was used to process the data and generate activity graphs (80).

Quantification of CFUs
Residual CFU counts were quantified as previously described (40). In brief, *Sal*-GFP–infected larvae (approximately 15 per sample) were homogenized, and the dissociated larval suspension was diluted 1:10, $1:10^3$, $1:10^5$, and $1:10^7$ and spot-plated in triplicate onto kanamycin-supplemented LB agar plates. After overnight incubation at 28°C, colonies were counted and CFUs were calculated.

In vitro mRNA transcription
Sense and antisense *per2* and *cry1a* expression constructs were amplified from cDNA using Phusion high-fidelity DNA polymerase (New England Biolabs) and primer pairs with incorporated Bam HI/Eco RI restriction sites (for *per2* constructs) and Xho I/Xba I restriction sites (for *cry1a* constructs) (see table S2 for oligonucleotide sequences). Amplicons were cloned into a Bam HI/Eco RI–linearized and Xho I/Xba I–linearized PCS2+ vector to generate *per2*/pCS2+, anti-*per2*/pCS2+, and *cry1a*/pCS2+, and anti-*cry1a*/pCS2+ expression vectors, respectively. Expression vectors were linearized with Apa I and transcribed using the mMESSAGE mMACHINE SP6

transcription kit (Ambion). To generate *bm1la-His* mRNA, the *bmal1a* pcDNA3.1/*myc*-His construct was digested with Sma I and transcribed using the mMESSAGE mMACHINE T7 transcription kit (Ambion).

Immunofluorescence
Immunofluorescence experiments were performed as previously described (46). In brief, larvae were fixed overnight in 4% paraformaldehyde (PFA) at 4°C before dehydration into 100% methanol. Samples were then rehydrated into PBTr [PBS supplemented with 0.65% (v/v) Triton X-100] and permeabilized with proteinase K (10 µg/ml in PBTr) for 30 min at RT. After fixation in 4% PFA for 20 min at RT, samples were incubated for 1 hour in blocking solution (PBTr supplemented with 10% normal goat serum) and incubated sequentially overnight in primary and secondary antibodies. The primary and secondary antibodies used for the detection of DsRED2, and mCherry and their dilutions were as follows: rabbit anti-DsRED (1:500; Takara Bio, catalog no. 632496) and goat anti-rabbit Alexa Fluor 546 (1:500; Thermo Fisher Scientific, catalog no. A-11035), mouse anti-mCherry (1:500; Takara Bio, catalog no. 632543), and goat anti-mouse Alexa Fluor 546 (1:500; Thermo Fisher Scientific, catalog no. A-11003).

Neutrophil tracking
For neutrophil tracking experiments, otic vesicles were injected with 600 CFU of *Sal*-GFP at 52 hpf (ZT4, LD condition), and the recruitment of neutrophils was immediately tracked for 1.5 hours by time-lapse confocal microscopy (z-stacks with 3-µm intervals were collected through the entire otic vesicle every minute). Track velocities, displacement rates, and meandering indices were calculated for individual neutrophil tracks using Fiji (81). Recruitment analysis was only performed on neutrophils that migrated from a starting position at least 100 µm from the otic vesicle border.

Live fluorescence microscopy
Larvae were anesthetized with 4% tricaine and arrayed in 3% methylcellulose in E3. Images were taken using a DS-U2/L2 camera fitted to a Nikon SMZ1500 fluorescence stereomicroscope (with a GFP-L filter set, excitation 480/40 nm) or a Zeiss Axio Zoom. V16 stereo microscope [with enhanced GFP (excitation 470/40 nm) and monomeric red fluorescent protein (excitation 572/25 nm) filter sets] equipped with a Zeiss Axiocam 506 mono camera.

Confocal microscopy
Live confocal imaging was performed with an Olympus Fluoview FV1000 laser scanning confocal microscope equipped with an incubation chamber set to 28°C. Anesthetized larvae were mounted in 1% (w/v) low–melting point agarose in E3 medium supplemented with 0.003% PTU and 3.2% tricaine. All imaging parameters were kept identical within, and across, imaging experiments when measuring neutrophil killing rates and quantifying CellROX fluorescence in bacteria-laden neutrophils (including zoom, pixel dimensions, laser voltage, gain, offset, pinhole size, and scanning speed). For immunofluorescence imaging, a Nikon C1 Eclipse confocal microscope was used.

Bacterial killing rates and ROS quantification
Neutrophil killing rates were measured at 3 to 4 hpi using time-lapse confocal microscopy as previously described (40). In brief, time-lapse imaging [z series (1.5-µm step size) collected every minute, 60×

objective] was performed on individual bacteria-laden neutrophils within infected larvae for approximately 10 min ($n = 6$ time-lapse movies per infection experiment). To be included in the dataset, there needed to be no evidence of additional bacterial phagocytosis over the imaging period, and the neutrophil was required to remain within the x, y, and z dimensions throughout the imaging period. Time-lapse movies were analyzed using Volocity v6.3 image analysis software. Volumes (μm^3) of intracellular *Sal*-GFP were measured at the beginning and end of each time-lapse movie with the volume measurement tool in Volocity using GFP fluorescence signal intensity (with a constant threshold setting). A region of interest (ROI) was manually positioned around the neutrophil in x, y, and z dimensions, and the sum of the volumes for all *Sal*-GFP objects within the ROI was quantified to give a total volume. From this, neutrophil killing rates were calculated as (initial volume – final volume)/time or $\Delta\mu m^3$/min.

The cell-permeable fluorescent probe CellROX Deep Red reagent (Life Sciences, Thermo Fisher Scientific) was used to measure ROS production in neutrophils as previously described (*40*). In brief, 2.5 nM CellROX was co-injected with *Sal*-GFP. Z-stacks (1.5-μm step size) of bacteria-laden neutrophils were imaged by confocal microscopy at 3 to 4 hpi. The total fluorescence intensity of CellROX within neutrophils was measured using Volocity v6.3. An ROI was drawn around individual bacteria-laden neutrophils in the x, y, and z dimensions. Using the threshold function (with a constant threshold setting) for the CellROX channel (excitation/emission maxima of 640/665 nm), the sum of the grayscale intensity values of individual voxels within the ROI was then measured and plotted as the total fluorescence intensity of CellROX per neutrophil (in arbitrary units).

Generating *ncf1* crispants
To generate F0 crispants lacking Ncf1 activity, injection mixes of 5 μM *ncf1* sgRNAs 1 and 2 (sourced from IDT using their predesigned library, design ID: Dr.Cas9.NCF1.1.AB and Dr.Cas9.NCF1.1.AA, respectively, and resuspended in sterile H$_2$O) + Cas9 protein (Alt-R *Streptococcus pyogenes* Cas9 nuclease, v.3, IDT) were incubated at 37°C for 5 min, as previously described (*82*). One nanoliter of the injection mix was injected into the cytoplasm of one-cell–stage *Tg*(*lyz:DsRED2*) embryos. To assess for targeted editing and to quantify editing efficiency, genomic DNA was isolated at 2 dpf using the HotShot method (*83*) for the T7 endonuclease I assay, Sanger sequencing of target-spanning amplicons, and NGS.

T7 endonuclease I assay
For initial testing of sgRNA editing, the T7 endonuclease I assay was used, as previously described (*84*). See table S2 for oligonucleotide sequences.

Quantification of CRISPR-Cas9 editing by NGS
To quantify the editing efficiencies of *ncf1*-, *hmgb1a*-, CNS4-, and *tyr*-targeting sgRNAs, NGS was performed on nested PCR amplicons. Primary PCRs were performed with the same primer pairs used for the T7 endonuclease I assay (see table S2 for oligonucleotide sequences) using Platinum SuperFi II DNA polymerase (Life Technologies, Thermo Fisher Scientific). For transgene-specific editing with CNS4 sgRNA1 and 2, transgene-specific primers were used (see table S2 for oligonucleotide sequences). A 1:250 dilution of the primary PCR was used as a template for a secondary PCR

using primer pairs with incorporated Illumina adaptor sequences (see table S2 for oligonucleotide sequences). After a final PCR with indexing primers, products were cleaned using AMPure XP Beads (Backman Coulter Life Sciences), as per the manufacturer's protocol, and sequenced on an Illumina MiSeq system. Indels were quantified from FASTQ sequencing files using the online sequence analysis tool CRISPResso2 (*85*), with a quantification window set at 20 nucleotides on either side of the predicted cleavage position.

Flow cytometry and FACS
Larvae were dissociated as previously described (*86*) or as follows. In brief, dechorionated larvae were dissociated in 10× trypsin-EDTA by constant pipetting for 5 min before addition of stop solution [20% fetal bovine serum (FBS) in PBS]. After centrifugation (1500*g* at 4°C), the cell pellet was gently resuspended into ice-cold PBS supplemented with 5% FBS and passed thorough 40-μm cell strainers (BD Falcon) three times. Cells were stored on ice for immediate flow cytometry or FACS. Flow quantification of neutrophils or macrophages from larvae was performed as described (*87*). Unless otherwise stated, cells were harvested from larvae at 52 hpf (ZT4 in the LD condition) for quantification using a BD LSR II flow cytometer, and cells were gated on the basis of forward and side scatter characteristics and DsRED2 or mCherry expression, respectively. Neutrophils, macrophages, and lens cells were FACS-isolated using a BD FACS Aria II or a Cytek Aurora CS cell sorter into PBS supplemented with 5% FBS for transplantation, 10× lysis buffer (Takara Bio) for RNA-seq (1000 cells per sample), RLT lysis buffer for immediate RNA purification and qRT-PCR (RNeasy Micro Kit, QIAGEN), and 8 mM NaOH for DNA extraction using the HotShot method, as previously described (*88*). When used for RNA-seq, neutrophils were isolated from the dissected heads of infected larvae to enrich for cells at the infection site.

Neutrophil transplantation
FACS-isolated neutrophils were transplanted as previously described (*44*). In brief, cells were sorted into a 1.5-ml microcentrifuge tube containing 20 μl of resuspension solution (9:1 Ringer's solution:PBS) at 4°C. Cells were then concentrated by centrifugation (260*g* for 10 min at 4°C) and resuspended in approximately 20 μl of resuspension solution. Neutrophils were FACS-isolated from 4-dpf *Tg* (*lyz:DsRED2*) and *Tg*(*lyz:DsRED2*);*per2^{nz90}* larvae (at ZT4 in the LD condition), the earliest time point when DsRED2 expression was sufficiently strong to visualize individual neutrophils when transplanting into age-matched recipients under fluorescence microscopy. Approximately 10 to 50 neutrophils per larva were delivered into the hindbrain ventricles of anaesthetized recipient larvae (immobilized in 3% methyl cellulose in E3 medium) using CellTram Oil (Eppendorf), and after a 1-day recovery period, 1000 CFU *Sal*-GFP was microinjected (at ZT4). Neutrophil killing rates and ROS measurements were then performed at 3 to 4 hpi.

RNA-seq and bioinformatics analysis
After sorting into 10× lysis buffer supplemented with ribonuclease inhibitor, cells were vortexed briefly to homogenize and lyse the cells, briefly centrifuged, and stored at −80°C. For cDNA synthesis, samples were thawed on ice before cDNA synthesis using the SMART-Seq v4 ultra low input RNA kit for sequencing (Takara Bio), as per the manufacturer's protocol. The cDNA from each sample was run on an Agilent 2100 Bioanalyzer to assess cDNA fragment

size, concentration, and purity, and 1 ng of cDNA was the input for each library using the Nextera XT DNA Library Preparation Kit (Illumina), as per the manufacturer's protocol. Libraries were checked for size distribution, purity, and concentration on an Agilent 2100 Bioanalyzer and then sequenced using a NextSeq 500 (75-bp single-end reads).

Single-end reads were checked for quality using FastQC, and cleaned reads were mapped to the zebrafish reference genome (GRCz10). Expression levels were measured as fragments per kilobase of transcript per million mapped reads using the Cuffquant and Cuffnorm components of Cufflinks software. DESeq was then used to reveal >DEGs between samples. The expression fold change ($\log_2$FC) was set to >1, and the false discovery rate (FDR) was set to <0.05 as screening criteria for DEGs. DEGs were functionally annotated using GO enrichment analysis. Analysis of RNA sequencing data was performed with assistance from CD genomics (www.cd-genomics.com/).

Morpholino injections

MO (Gene Tools) were resuspended in sterile water and injected into one-cell–stage embryos. Efficacious doses for MOs were determined empirically. RT-PCR was used to determine MO specificity. The MO sequences (and doses/embryo) were as follows: control MO (5′-CCTCTTACCTCAGTTACAATTTATA-3′) (0.5 pmol) and *hmgb1a* splice-blocking MO (5′-AATGAGAGGTGTGACTGAC-CTTCC-3′) (0.5 pmol).

Neutrophil-specific CRISPR-Cas9 editing

Neutrophil-targeted editing was carried out as previously described (*47*, *88*), with modifications. The *hmgb1a* sgRNA [sourced from Integrated DNA Technologies (IDT) using their predesigned library, design ID: Dr.Cas9.HMGB1A.1.AB], CNS4 sgRNAs 1 and 2 (sourced from IDT using their custom design service), and *tyr* sgRNA (sourced from IDT using their predesigned library, design ID: Dr.Cas9.TYR.1.AA) were resuspended in sterile H_2O at 100 μM. All sgRNAs were first evaluated for targeted editing in whole larvae using the T7 endonuclease I assay and/or Sanger sequencing. In brief, sgRNA:Cas9 RNP complexes were generated for each sgRNA by incubating a 5 μM sgRNA + Cas9 protein (Alt-R *Streptococcus pyogenes* Cas9 nuclease, v.3, IDT) mix at 37°C for 5 min, as previously described (*82*). One nanoliter of the injection mix was injected into the cytoplasm of one-cell–stage WT embryos. At 2 dpf, genomic DNA was isolated using the HotShot method (*83*) for the T7 endonuclease I assay and/or PCR and Sanger sequencing of target-spanning amplicons. For neutrophil-specific editing, 1 nl of a 5-μM sgRNA injection mix was similarly injected into the cytoplasm of one-cell–stage *Tg(lyz:nls-cas9);Tg(lyzDsRED2)* embryos. As controls for *hmgb1a*, CNS4, and *tyr* editing, sgRNAs were injected into *Tg(lyz:DsRED2)* embryos. Targeted editing was evaluated using the T7 endonuclease I assay, Sanger sequencing, and NGS from FACS-isolated neutrophils at 2 dpf.

Site-directed mutagenesis

To create the *per2_CBDdel*/pCS2+ expression construct and *per2_CBDdel*/pENTR/D-TOPO middle-entry vector (to generate the *lyz:per2_CBDdel* transgene construct), site-directed mutagenesis was performed using the Q5 site-directed mutagenesis kit (New England Biolabs), with slight modifications. In brief, *per2*/pCS2$^+$ and *per2*/pENTR/D-TOPO vectors were used as templates for high-fidelity PCR reactions using Platinum SuperFi II DNA polymerase (Life Technologies, Thermo Fisher Scientific), and forward and reverse primers were designed to exclude the CBD of *per2* (amino acid residues 1268 to 1382) (see table S2 for oligonucleotide sequences). After Dpn I digestion of dam-methylated template DNA and amplicon religation with the Quick Ligation kit (New England Biolabs), mutagenesis success was verified by Sanger sequencing.

Generation of *per2*, *per2_CBDdel*, and *bmal1a* pcDNA3.1/*myc*-His expression constructs and protein immunoblotting

To generate the *per2* and *per2_CBDdel* pcDNA3.1/*myc*-His expression constructs, the *lyz:per2* and *lyz:per2_CBDdel* transgene constructs were used as templates for PCR reactions using Platinum SuperFi II DNA polymerase (Life Technologies, Thermo Fisher Scientific) and forward and reverse primers with incorporated Kpn I and Apa I restriction sites and designed to lack the *per2* stop codon (see table S2 for oligonucleotide sequences). The resulting amplicons were cloned into the pCRBlunt II-TOPO vector (Life Technologies, Thermo Fisher Scientific), sequence verified, and subcloned in-frame into Kpn I/Apa I–linearized pcDNA3.1/*myc*-His mammalian expression vector (Thermo Fisher Scientific). To create the *bmal1a* pcDNA3.1/*myc*-His expression construct, the same cloning strategy was used using cDNAs generated from 2-dpf larvae as a template. For protein immunoblotting, human embryonic kidney–293T cells were transfected with *per2*, *per2_CBDdel*, *bmal1a* pcDNA3.1/*myc*-His vectors or an empty pcDNA3.1 vector using Fugene HD transfection reagent (Promega), as per the manufacturer's instructions. Forty-eight hours after transfection, cells were lyzed in radioimmunoprecipitation assay buffer supplemented with 1× protease inhibitors (Roche) and separated by SDS–polyacrylamide gel electrophoresis followed by protein immunoblot analysis using 6×-His Tag polyclonal antibody (PA1-983B, Thermo Fisher Scientific) or anti-vimentin monoclonal antibody (M0725, Dako) and visualized on a ChemiDoc Touch imaging system (Bio-Rad).

VISTA sequence alignment and JASPAR analysis of TF binding motifs

Sequences for HMGB1 orthologs were obtained from Ensembl, and sequence alignments were performed using VISTA (http://genome.lbl.gov/vista/index.shtml) and the Shuffle-LAGAN alignment program. Conservation peaks denote >50% identified conservation within a 25-bp sliding window and a minimum conservation width of 75 bp. Putative binding profiles for CLOCK, BMAL1, and NF-κB were identified within each CNS using JASPAR (https://jaspar.genereg.net/) (*89*).

ChIP-qPCR assay

ChIP assays were performed using the Millipore ChIP assay kit (17-295, Millipore), as per the manufacturer's instructions. In brief, 100 1-dpf *bma1a-His* mRNA (100 pg per embryo)– or PBS-injected embryos were fixed in 2% formaldehyde at room temperature for 30 min. A $1/_{10}$ volume of 1.25 M glycine was then added in inhibit cross-linking followed by three 10-min washes in PBS. Subsequent steps were carried out as per the manufacturer's instructions (Millipore). Chromatin was sonicated using a Bioruptor Pico sonication device (Diagenode) for 10 cycles using a 30-s (on) and 30-s (off) setting to a size range of 100 to 1000 bps, as detected using an Agilent Tapesation system with a D1000 ScreenTape (Agilent Technologies). Chromatin was immunoprecipitated with 6×-His Tag polyclonal

antibody (PA1-983B, Thermo Fisher Scientific) or rabbit immuno-globulin G (IgG) isotype control antibody (31235, Thermo Fisher Scientific). Quantitative PCR was performed with ChIP and input DNA using primers specific to *hmgb1a* CNS4 or *ef1a* as control (see table S2 for oligonucleotide sequences). Data from three experimental replicates were plotted as percentage of input.

Whole-mount in situ hybridization analysis

For riboprobe synthesis, the full-length ORF for *hmgb1a* was PCR amplified from cDNAs generated from WT larvae (see table S2 for oligonucleotide sequences). The resulting amplicon was cloned into the pCRII-TOPO vector (Life Technologies, Thermo Fisher Scientific), and after linearization with Spe I digestion, riboprobes were synthesized using the T7 digoxigenin (DIG) RNA labeling kit (Roche), as per the manufacturer's protocol. Whole-mount in situ hybridization was performed as previously described (*90*). In brief, larvae were fixed in 4% PFA and permeabilized with proteinase K (10 μg/ml) for 1 hour. After fixation in 4% PFA (20 min at room temperature) and prehybridization, larvae were incubated with denatured DIG-labeled riboprobes at 65°C overnight and incubated with alkaline phosphatase-conjugated anti-DIG antibody (Roche). Staining was performed using BM Purple (Roche) as the substrate. After staining, larvae were fixed in 4% PFA and stored in 100% glycerol at 4°C.

Oxford nanopore sequencing

Genomic DNA was isolated from 50 WT or CNS4 sgRNA2 + Cas9-injected 2-dpf larvae using the DNeasy blood and tissue kit (QIAGEN) and cleaned using the Genomic DNA Clean and Concentrator kit (Zymo Research) as per the manufacturer's instructions. Genomic DNA quality was assessed using an Agilent Tapesation system with a Genomic DNA ScreenTape (Agilent Technologies), and quantity was measured using a Qubit 3.0 fluorometer (Life Technologies). Sequencing libraries were prepared using the ligation sequencing kit V14 (SQKLSK114) according to the manufacturer's instructions (Oxford Nanopore Technologies). The libraries were run on an R10.4.1 PromethION flowcell (FLO-PR0114M; Oxford Nanopore Technologies). Super-accuracy live base calling was performed using Dorado v7.4.12. The total yield of sequencing data for WT larvae was 40.036 gigabytes, divided over 5,297,348 reads with a read N50 of 15.4 kilobytes and for CNS4 sgRNA2 + Cas9-injected larvae, was 35.485 gigabytes divided over 4,125,764 reads with a read N50 of 14.7 kilobytes.

Statistics

Data are presented as the mean ± SD or SE (as described in the figure legends). Statistical significance of differences between two groups was determined using an unpaired Student's *t* test, and for multiple comparisons, a one-way analysis of variance (ANOVA) with Dunnett's post hoc correction was used. For temporal analysis of gene expression between WT, *per2*[nz90], and *cry1a*[nz91] groups, Kaplan-Meier survival comparisons, two-way ANOVA with Bonferroni's post-test, and Gehan-Breslow-Wilcoxon tests were used, respectively. *P* values of less than 0.05 were considered statistically significant. All statistical analyses were performed using GraphPad Prism 8.0 (GraphPad Software).

Supplementary Materials

The PDF file includes:
Figs. S1 to S11
Tables S1 and S2

Other Supplementary Material for this manuscript includes the following:
Data files S1 and S2
MDAR Reproducibility Checklist

REFERENCES AND NOTES

1. T. Roenneberg, M. Merrow, Circadian clocks—The fall and rise of physiology. *Nat. Rev. Mol. Cell Biol.* **6**, 965–971 (2005).
2. A. M. Curtis, M. M. Bellet, P. Sassone-Corsi, L. A. O'Neill, Circadian clock proteins and immunity. *Immunity* **40**, 178–186 (2014).
3. C. Scheiermann, Y. Kunisaki, P. S. Frenette, Circadian control of the immune system. *Nat. Rev. Immunol.* **13**, 190–198 (2013).
4. C. Wang, L. K. Lutes, C. Barnoud, C. Scheiermann, The circadian immune system. *Sci. Immunol.* **7**, eabm2465 (2022).
5. C. Scheiermann, J. Gibbs, L. Ince, A. Loudon, Clocking in to immunity. *Nat. Rev. Immunol.* **18**, 423–437 (2018).
6. M. Akashi, A. Okamoto, Y. Tsuchiya, T. Todo, E. Nishida, K. Node, A positive role for PERIOD in mammalian circadian gene expression. *Cell Rep.* **7**, 1056–1064 (2014).
7. R. Ye, C. P. Selby, Y. Y. Chiou, I. Ozkan-Dagliyan, S. Gaddameedhi, A. Sancar, Dual modes of CLOCK:BMAL1 inhibition mediated by cryptochrome and period proteins in the mammalian circadian clock. *Genes Dev.* **28**, 1989–1998 (2014).
8. R. Ye, C. P. Selby, N. Ozturk, Y. Annayev, A. Sancar, Biochemical analysis of the canonical model for the mammalian circadian clock. *J. Biol. Chem.* **286**, 25891–25902 (2011).
9. M. M. Bellet, E. Deriu, J. Z. Liu, B. Grimaldi, C. Blaschitz, M. Zeller, R. A. Edwards, S. Sahar, S. Dandekar, P. Baldi, M. D. George, M. Raffatellu, P. Sassone-Corsi, Circadian clock regulates the host response to *Salmonella*. *Proc. Natl. Acad. Sci. U.S.A.* **110**, 9897–9902 (2013).
10. A. C. Silver, A. Arjona, W. E. Walker, E. Fikrig, The circadian clock controls toll-like receptor 9-mediated innate and adaptive immunity. *Immunity* **36**, 251–261 (2012).
11. J. O. Early, D. Menon, C. A. Wyse, M. P. Cervantes-Silva, Z. Zaslona, R. G. Carroll, E. M. Palsson-McDermott, S. Angiari, D. G. Ryan, S. E. Corcoran, G. Timmons, S. S. Geiger, D. J. Fitzpatrick, D. O'Connell, R. J. Xavier, K. Hokamp, L. A. J. O'Neill, A. M. Curtis, Circadian clock protein BMAL1 regulates IL-1β in macrophages via NRF2. *Proc. Natl. Acad. Sci. U.S.A.* **115**, E8460–E8468 (2018).
12. M. Hayashi, S. Shimba, M. Tezuka, Characterization of the molecular clock in mouse peritoneal macrophages. *Biol. Pharm. Bull.* **30**, 621–626 (2007).
13. R. Narasimamurthy, M. Hatori, S. K. Nayak, F. Liu, S. Panda, I. M. Verma, Circadian clock protein cryptochrome regulates the expression of proinflammatory cytokines. *Proc. Natl. Acad. Sci. U.S.A.* **109**, 12662–12667 (2012).
14. D. Druzd, O. Matveeva, L. Ince, U. Harrison, W. He, C. Schmal, H. Herzel, A. H. Tsang, N. Kawakami, A. Leliavski, O. Uhl, L. Yao, L. E. Sander, C. S. Chen, K. Kraus, A. de Juan, S. M. Hergenhan, M. Ehlers, B. Koletzko, R. Haas, W. Solbach, H. Oster, C. Scheiermann, Lymphocyte circadian clocks control lymph node trafficking and adaptive immune responses. *Immunity* **46**, 120–132 (2017).
15. C. Wang, C. Barnoud, M. Cenerenti, M. Sun, I. Caffa, B. Kizil, R. Bill, Y. Liu, R. Pick, L. Garnier, O. A. Gkountidi, L. M. Ince, S. Holtkamp, N. Fournier, O. Michielin, D. E. Speiser, S. Hugues, A. Nencioni, M. J. Pittet, C. Jandus, C. Scheiermann, Dendritic cells direct circadian anti-tumour immune responses. *Nature* **614**, 136–143 (2023).
16. K. D. Nguyen, S. J. Fentress, Y. Qiu, K. Yun, J. S. Cox, A. Chawla, Circadian gene *Bmal1* regulates diurnal oscillations of Ly6C^{hi} inflammatory monocytes. *Science* **341**, 1483–1488 (2013).
17. S. J. Holtkamp, L. M. Ince, C. Barnoud, M. T. Schmitt, F. Sinturel, V. Pilorz, R. Pick, S. Jemelin, M. Muhlstadt, W. H. Boehncke, J. Weber, D. Laubender, J. Philippou-Massier, C. S. Chen, L. Holtermann, D. Vestweber, M. Sperandio, B. U. Schraml, C. Halin, C. Dibner, H. Oster, J. Renkawitz, C. Scheiermann, Circadian clocks guide dendritic cells into skin lymphatics. *Nat. Immunol.* **22**, 1375–1381 (2021).
18. J. R. Beytebiere, A. J. Trott, B. J. Greenwell, C. A. Osborne, H. Vitet, J. Spence, S. H. Yoo, Z. Chen, J. S. Takahashi, N. Ghaffari, J. S. Menet, Tissue-specific BMAL1 cistromes reveal that rhythmic transcription is associated with rhythmic enhancer-enhancer interactions. *Genes Dev.* **33**, 294–309 (2019).
19. J. Mermet, J. Yeung, C. Hurni, D. Mauvoisin, K. Gustafson, C. Jouffe, D. Nicolas, Y. Emmenegger, C. Gobet, P. Franken, F. Gachon, F. Naef, Clock-dependent chromatin topology modulates circadian transcription and behavior. *Genes Dev.* **32**, 347–358 (2018).
20. J. S. Menet, S. Pescatore, M. Rosbash, CLOCK:BMAL1 is a pioneer-like transcription factor. *Genes Dev.* **28**, 8–13 (2014).
21. L. Aguilar-Arnal, P. Sassone-Corsi, Chromatin landscape and circadian dynamics: Spatial and temporal organization of clock transcription. *Proc. Natl. Acad. Sci. U.S.A.* **112**, 6863–6870 (2015).
22. J. A. Ripperger, U. Schibler, Rhythmic CLOCK-BMAL1 binding to multiple E-box motifs drives circadian *Dbp* transcription and chromatin transitions. *Nat. Genet.* **38**, 369–374 (2006).
23. A. J. Trott, J. S. Menet, Regulation of circadian clock transcriptional output by CLOCK:BMAL1. *PLOS Genet.* **14**, e1007156 (2018).

24. O. Soehnlein, L. Lindbom, Phagocyte partnership during the onset and resolution of inflammation. *Nat. Rev. Immunol.* **10**, 427–439 (2010).

25. M. Casanova-Acebes, C. Pitaval, L. A. Weiss, C. Nombela-Arrieta, R. Chèvre, N. A-González, Y. Kunisaki, D. Zhang, N. van Rooijen, L. E. Silberstein, C. Weber, T. Nagasawa, P. S. Frenette, A. Castrillo, A. Hidalgo, Rhythmic modulation of the hematopoietic niche through neutrophil clearance. *Cell* **153**, 1025–1035 (2013).

26. W. He, S. Holtkamp, S. M. Hergenhan, K. Kraus, A. de Juan, J. Weber, P. Bradfield, J. M. P. Grenier, J. Pelletier, D. Druzd, C. S. Chen, L. M. Ince, S. Bierschenk, R. Pick, M. Sperandio, M. Aurrand-Lions, C. Scheiermann, Circadian expression of migratory factors establishes lineage-specific signatures that guide the homing of leukocyte subsets to tissues. *Immunity* **49**, 1175–1190.e7 (2018).

27. J. M. Adrover, C. Del Fresno, G. Crainiciuc, M. I. Cuartero, M. Casanova-Acebes, L. A. Weiss, H. Huerga-Encabo, C. Silvestre-Roig, J. Rossaint, I. Cossio, A. V. Lechuga-Vieco, J. Garcia-Prieto, M. Gomez-Parrizas, J. A. Quintana, I. Ballesteros, S. Martin-Salamanca, A. Aroca-Crevillen, S. Z. Chong, M. Evrard, K. Balabanian, J. Lopez, K. Bidzhekov, F. Bachelerie, F. Abad-Santos, C. Munoz-Calleja, A. Zarbock, O. Soehnlein, C. Weber, L. G. Ng, C. Lopez-Rodriguez, D. Sancho, M. A. Moro, B. Ibanez, A. Hidalgo, A neutrophil timer coordinates immune defense and vascular protection. *Immunity* **50**, 390–402.e10 (2019).

28. B. Uhl, Y. Vadlau, G. Zuchtriegel, K. Nekolla, K. Sharaf, F. Gaertner, S. Massberg, F. Krombach, C. A. Reichel, Aged neutrophils contribute to the first line of defense in the acute inflammatory response. *Blood* **128**, 2327–2337 (2016).

29. F. Ellett, L. Pase, J. W. Hayman, A. Andrianopoulos, G. J. Lieschke, *mpeg1* promoter transgenes direct macrophage-lineage expression in zebrafish. *Blood* **117**, e49–e56 (2011).

30. S. A. Renshaw, C. A. Loynes, D. M. Trushell, S. Elworthy, P. W. Ingham, M. K. Whyte, A transgenic zebrafish model of neutrophilic inflammation. *Blood* **108**, 3976–3978 (2006).

31. C. Hall, M. V. Flores, T. Storm, K. Crosier, P. Crosier, The zebrafish lysozyme C promoter drives myeloid-specific expression in transgenic fish. *BMC Dev. Biol.* **7**, 42 (2007).

32. J. R. Mathias, B. J. Perrin, T. X. Liu, J. Kanki, A. T. Look, A. Huttenlocher, Resolution of inflammation by retrograde chemotaxis of neutrophils in transgenic zebrafish. *J. Leukoc. Biol.* **80**, 1281–1288 (2006).

33. I. A. Froland Steindal, D. Whitmore, Circadian clocks in fish—what have we learned so far? *Biology* **8**, 17 (2019).

34. M. L. Idda, C. Bertolucci, D. Vallone, Y. Gothilf, F. J. Sanchez-Vazquez, N. S. Foulkes, Circadian clocks: Lessons from fish. *Prog. Brain Res.* **199**, 41–57 (2012).

35. L. Y. Du, H. Darroch, P. Keerthisinghe, E. Ashimbayeva, J. W. Astin, K. E. Crosier, P. S. Crosier, G. Warman, J. Cheeseman, C. J. Hall, The innate immune cell response to bacterial infection in larval zebrafish is light-regulated. *Sci. Rep.* **7**, 12657 (2017).

36. B. Zheng, D. W. Larkin, U. Albrecht, Z. S. Sun, M. Sage, G. Eichele, C. C. Lee, A. Bradley, The mPer2 gene encodes a functional component of the mammalian circadian clock. *Nature* **400**, 169–173 (1999).

37. S. Lykke-Andersen, T. H. Jensen, Nonsense-mediated mRNA decay: An intricate machinery that shapes transcriptomes. *Nat. Rev. Mol. Cell Biol.* **16**, 665–677 (2015).

38. M. Wang, Z. Zhong, Y. Zhong, W. Zhang, H. Wang, The zebrafish period2 protein positively regulates the circadian clock through mediation of retinoic acid receptor (RAR)-related orphan receptor α (Rorα). *J. Biol. Chem.* **290**, 4367–4382 (2015).

39. H. Darroch, P. Keerthisinghe, Y. J. Sung, L. Rolland, A. Prankerd-Gough, P. S. Crosier, J. W. Astin, C. J. Hall, Infection-experienced HSPCs protect against infections by generating neutrophils with enhanced mitochondrial bactericidal activity. *Sci. Adv.* **9**, eadf9904 (2023).

40. J. W. Astin, P. Keerthisinghe, L. Du, L. E. Sanderson, K. E. Crosier, P. S. Crosier, C. J. Hall, Innate immune cells and bacterial infection in zebrafish. *Methods Cell Biol.* **138**, 31–60 (2017).

41. W. M. Nauseef, The phagocyte NOX2 NADPH oxidase in microbial killing and cell signaling. *Curr. Opin. Immunol.* **60**, 130–140 (2019).

42. A. Panday, M. K. Sahoo, D. Osorio, S. Batra, NADPH oxidases: An overview from structure to innate immunity-associated pathologies. *Cell. Mol. Immunol.* **12**, 5–23 (2015).

43. J. El-Benna, P. M. Dang, M. A. Gougerot-Pocidalo, J. C. Marie, F. Braut-Boucher, p47phox, the phagocyte NADPH oxidase/NOX2 organizer: Structure, phosphorylation and implication in diseases. *Exp. Mol. Med.* **41**, 217–225 (2009).

44. H. Darroch, J. W. Astin, C. J. Hall, Isolation of neutrophils from larval zebrafish and their transplantation into recipient larvae for functional studies. *Methods Mol. Biol.* **2087**, 61–75 (2020).

45. D. Tang, R. Kang, H. J. Zeh, M. T. Lotze, The multifunctional protein HMGB1: 50 years of discovery. *Nat. Rev. Immunol.* **23**, 824–841 (2023).

46. C. J. Hall, R. H. Boyle, J. W. Astin, M. V. Flores, S. H. Oehlers, L. E. Sanderson, F. Ellett, G. J. Lieschke, K. E. Crosier, P. S. Crosier, Immunoresponsive gene 1 augments bactericidal activity of macrophage-lineage cells by regulating β-oxidation-dependent mitochondrial ROS production. *Cell Metab.* **18**, 265–278 (2013).

47. Y. Wang, A. Y. Hsu, E. M. Walton, S. J. Park, R. Syahirah, T. Wang, W. Zhou, C. Ding, A. P. Lemke, G. Zhang, D. M. Tobin, Q. Deng, A robust and flexible CRISPR/Cas9-based system for neutrophil-specific gene inactivation in zebrafish. *J. Cell Sci.* **134**, (2021).

48. P. Haffter, J. Odenthal, M. C. Mullins, S. Lin, M. J. Farrell, E. Vogelsang, F. Haas, M. Brand, F. J. van Eeden, M. Furutani-Seiki, M. Granato, M. Hammerschmidt, C. P. Heisenberg, Y. J. Jiang, D. A. Kane, R. N. Kelsh, N. Hopkins, C. Nusslein-Volhard, Mutations affecting pigmentation and shape of the adult zebrafish. *Dev. Genes Evol.* **206**, 260–276 (1996).

49. H. M. Isles, C. A. Loynes, S. Alasmari, F. C. Kon, K. M. Henry, A. Kadochnikova, J. Hales, C. F. Muir, M. C. Keightley, V. Kadirkamanathan, N. Hamilton, G. J. Lieschke, S. A. Renshaw, P. M. Elks, Pioneer neutrophils release chromatin within in vivo swarms. *eLife* **10**, e68755 (2021).

50. D. Baranasic, M. Hörtenhuber, P. J. Balwierz, T. Zehnder, A. K. Mukarram, C. Nepal, C. Várnai, Y. Hadzhiev, A. Jimenez-Gonzalez, N. Li, J. Wragg, F. M. D'Orazio, D. Relic, M. Pachkov, N. Díaz, B. Hernández-Rodríguez, Z. Chen, M. Stoiber, M. Dong, I. Stevens, S. E. Ross, A. Eagle, R. Martin, O. Obasaju, S. Rastegar, A. C. M. Garvey, W. Kopp, E. Chambers, D. Wang, H. R. Kim, R. D. Acemel, S. Naranjo, M. Łapiński, V. Chong, S. Mathavan, B. Peers, T. Sauka-Spengler, M. Vingron, P. Carninci, U. Ohler, S. A. Lacadie, S. M. Burgess, C. Winata, F. van Eeden, J. M. Vaquerizas, J. L. Gómez-Skarmeta, D. Onichtchouk, B. J. Brown, O. Bogdanovic, E. van Nimwegen, M. Westerfield, F. C. Wardle, C. O. Daub, B. Lenhard, F. Müller, Multiomic atlas with functional stratification and developmental dynamics of zebrafish cis-regulatory elements. *Nat. Genet.* **54**, 1037–1050 (2022).

51. S. Moleri, G. Cappellano, G. Gaudenzi, S. Cermenati, F. Cotelli, D. S. Horner, M. Beltrame, The HMGB protein gene family in zebrafish: Evolution and embryonic expression patterns. *Gene Expr. Patterns* **11**, 3–11 (2011).

52. R. Gordan, N. Shen, I. Dror, T. Zhou, J. Horton, R. Rohs, M. L. Bulyk, Genomic regions flanking E-box binding sites influence DNA binding specificity of bHLH transcription factors through DNA shape. *Cell Rep.* **3**, 1093–1104 (2013).

53. Y. Gothilf, R. Toyama, S. L. Coon, S. J. Du, I. B. Dawid, D. C. Klein, Pineal-specific expression of green fluorescent protein under the control of the serotonin-N-acetyltransferase gene regulatory regions in transgenic zebrafish. *Dev. Dyn.* **225**, 241–249 (2002).

54. L. Appelbaum, D. Vallone, A. Anzulovich, L. Ziv, M. Tom, N. S. Foulkes, Y. Gothilf, Zebrafish arylalkylamine-N-acetyltransferase genes—Targets for regulation of the circadian clock. *J. Mol. Endocrinol.* **36**, 337–347 (2006).

55. J. Gibbs, L. Ince, L. Matthews, J. Mei, T. Bell, N. Yang, B. Saer, N. Begley, T. Poolman, M. Pariollaud, S. Farrow, F. DeMayo, T. Hussell, G. S. Worthen, D. Ray, A. Loudon, An epithelial circadian clock controls pulmonary inflammation and glucocorticoid action. *Nat. Med.* **20**, 919–926 (2014).

56. S. R. Lundy, T. Ahmad, T. Simoneaux, I. Benyeogor, Y. Robinson, Z. George, D. Ellerson, W. Kirlin, T. Omosun, F. O. Eko, C. M. Black, U. Blas-Machado, J. P. DeBruyne, J. U. Igietseme, Q. He, Y. O. Omosun, Effect of time of day of infection on chlamydia infectivity and pathogenesis. *Sci. Rep.* **9**, 11405 (2019).

57. N. Borregaard, Neutrophils, from marrow to microbes. *Immunity* **33**, 657–670 (2010).

58. E. Kolaczkowska, P. Kubes, Neutrophil recruitment and function in health and inflammation. *Nat. Rev. Immunol.* **13**, 159–175 (2013).

59. R. S. Flannagan, G. Cosio, S. Grinstein, Antimicrobial mechanisms of phagocytes and bacterial evasion strategies. *Nat. Rev. Microbiol.* **7**, 355–366 (2009).

60. M. T. Lotze, K. J. Tracey, High-mobility group box 1 protein (HMGB1): Nuclear weapon in the immune arsenal. *Nat. Rev. Immunol.* **5**, 331–342 (2005).

61. H. Yang, D. J. Antoine, U. Andersson, K. J. Tracey, The many faces of HMGB1: Molecular structure-functional activity in inflammation, apoptosis, and chemotaxis. *J. Leukoc. Biol.* **93**, 865–873 (2013).

62. T. Chavakis, A. Bierhaus, N. Al-Fakhri, D. Schneider, S. Witte, T. Linn, M. Nagashima, J. Morser, B. Arnold, K. T. Preissner, P. P. Nawroth, The pattern recognition receptor (RAGE) is a counterreceptor for leukocyte integrins: A novel pathway for inflammatory cell recruitment. *J. Exp. Med.* **198**, 1507–1515 (2003).

63. C. J. Treutiger, G. E. Mullins, A. S. Johansson, A. Rouhiainen, H. M. Rauvala, H. Erlandsson-Harris, U. Andersson, H. Yang, K. J. Tracey, J. Andersson, J. E. Palmblad, High mobility group 1 B-box mediates activation of human endothelium. *J. Intern. Med.* **254**, 375–385 (2003).

64. J. Fan, Y. Li, R. M. Levy, J. J. Fan, D. J. Hackam, Y. Vodovotz, H. Yang, K. J. Tracey, T. R. Billiar, M. A. Wilson, Hemorrhagic shock induces NAD(P)H oxidase activation in neutrophils: Role of HMGB1-TLR4 signaling. *J. Immunol.* **178**, 6573–6580 (2007).

65. K.-H. Wei, I.-T. Lin, K. Chowdhury, K. L. Lim, K.-T. Liu, T.-M. Ko, Y.-M. Chang, K.-C. Yang, S.-L. B. Lai, Comparative single-cell profiling reveals distinct cardiac resident macrophages essential for zebrafish heart regeneration. *eLife* **12**, e84679 (2023).

66. C. Summers, S. M. Rankin, A. M. Condliffe, N. Singh, A. M. Peters, E. R. Chilvers, Neutrophil kinetics in health and disease. *Trends Immunol.* **31**, 318–324 (2010).

67. J. S. Menet, J. Rodriguez, K. C. Abruzzi, M. Rosbash, Nascent-Seq reveals novel features of mouse circadian transcriptional regulation. *eLife* **1**, e00011 (2012).

68. J. Yeung, F. Naef, Rhythms of the genome: Circadian dynamics from chromatin topology, tissue-specific gene expression, to behavior. *Trends Genet.* **34**, 915–926 (2018).

69. N. Koike, S. H. Yoo, H. C. Huang, V. Kumar, C. Lee, T. K. Kim, J. S. Takahashi, Transcriptional architecture and chromatin landscape of the core circadian clock in mammals. *Science* **338**, 349–354 (2012).

70. G. Rey, F. Cesbron, J. Rougemont, H. Reinke, M. Brunner, F. Naef, Genome-wide and phase-specific DNA-binding rhythms of BMAL1 control circadian output functions in mouse liver. *PLoS Biol.* **9**, e1000595 (2011).

71. M. Blanter, M. Gouwy, S. Struyf, Studying neutrophil function in vitro: Cell models and environmental factors. *J. Inflamm. Res.* **14**, 141–162 (2021).

72. G. L. Burn, A. Foti, G. Marsman, D. F. Patel, A. Zychlinsky, The neutrophil. *Immunity* **54**, 1377–1391 (2021).

73. M. C. Gomes, D. Brokatzky, M. K. Bielecka, F. C. Wardle, S. Mostowy, *Shigella* induces epigenetic reprogramming of zebrafish neutrophils. *Sci. Adv.* **9**, eadf9706 (2023).

74. J. M. Davison, C. M. Akitake, M. G. Goll, J. M. Rhee, N. Gosse, H. Baier, M. E. Halpern, S. D. Leach, M. J. Parsons, Transactivation from Gal4-VP16 transgenic insertions for tissue-specific cell labeling and ablation in zebrafish. *Dev. Biol.* **304**, 811–824 (2007).

75. K. Labun, T. G. Montague, M. Krause, Y. N. T. Cleuren, H. Tjeldnes, E. Valen, CHOPCHOP v3: Expanding the CRISPR web toolbox beyond genome editing. *Nucleic Acids Res.* **47**, W171–W174 (2019).

76. L. E. Jao, S. R. Wente, W. Chen, Efficient multiplex biallelic zebrafish genome editing using a CRISPR nuclease system. *Proc. Natl. Acad. Sci. U.S.A.* **110**, 13904–13909 (2013).

77. K. M. Kwan, E. Fujimoto, C. Grabher, B. D. Mangum, M. E. Hardy, D. S. Campbell, J. M. Parant, H. J. Yost, J. P. Kanki, C. B. Chien, The Tol2kit: A multisite gateway-based construction kit for Tol2 transposon transgenesis constructs. *Dev. Dyn.* **236**, 3088–3099 (2007).

78. R. Y. Birnbaum, E. J. Clowney, O. Agamy, M. J. Kim, J. Zhao, T. Yamanaka, Z. Pappalardo, S. L. Clarke, A. M. Wenger, L. Nguyen, F. Gurrieri, D. B. Everman, C. E. Schwartz, O. S. Birk, G. Bejerano, S. Lomvardas, N. Ahituv, Coding exons function as tissue-specific enhancers of nearby genes. *Genome Res.* **22**, 1059–1068 (2012).

79. A. Vazquez-Torres, J. Jones-Carson, A. J. Baumler, S. Falkow, R. Valdivia, W. Brown, M. Le, R. Berggren, W. T. Parks, F. C. Fang, Extraintestinal dissemination of *Salmonella* by CD18-expressing phagocytes. *Nature* **401**, 804–808 (1999).

80. nzmattgrant, nzmattgrant/ZebraFishDataAnalysis: published version, version 1.0.0, Zenodo (2025); https://doi.org/10.5281/zenodo.15122276.

81. J. Schindelin, I. Arganda-Carreras, E. Frise, V. Kaynig, M. Longair, T. Pietzsch, S. Preibisch, C. Rueden, S. Saalfeld, B. Schmid, J. Y. Tinevez, D. J. White, V. Hartenstein, K. Eliceiri, P. Tomancak, A. Cardona, Fiji: An open-source platform for biological-image analysis. *Nat. Methods* **9**, 676–682 (2012).

82. K. Hoshijima, M. J. Jurynec, D. Klatt Shaw, A. M. Jacobi, M. A. Behlke, D. J. Grunwald, Highly efficient CRISPR-Cas9-based methods for generating deletion mutations and f0 embryos that lack gene function in zebrafish. *Dev. Cell* **51**, 645–657.e4 (2019).

83. N. D. Meeker, S. A. Hutchinson, L. Ho, N. S. Trede, Method for isolation of PCR-ready genomic DNA from zebrafish tissues. *Biotechniques* **43**, 610–614 (2007).

84. D. Y. Guschin, A. J. Waite, G. E. Katibah, J. C. Miller, M. C. Holmes, E. J. Rebar, A rapid and general assay for monitoring endogenous gene modification. *Methods Mol. Biol.* **649**, 247–256 (2010).

85. K. Clement, H. Rees, M. C. Canver, J. M. Gehrke, R. Farouni, J. Y. Hsu, M. A. Cole, D. R. Liu, J. K. Joung, D. E. Bauer, L. Pinello, CRISPResso2 provides accurate and rapid genome editing sequence analysis. *Nat. Biotechnol.* **37**, 224–226 (2019).

86. L. Covassin, J. D. Amigo, K. Suzuki, V. Teplyuk, J. Straubhaar, N. D. Lawson, Global analysis of hematopoietic and vascular endothelial gene expression by tissue specific microarray profiling in zebrafish. *Dev. Biol.* **299**, 551–562 (2006).

87. C. Hall, M. V. Flores, A. Chien, A. Davidson, K. Crosier, P. Crosier, Transgenic zebrafish reporter lines reveal conserved Toll-like receptor signaling potential in embryonic myeloid leukocytes and adult immune cell lineages. *J. Leukoc. Biol.* **85**, 751–765 (2009).

88. A. I. Isiaku, Z. Zhang, V. Pazhakh, H. R. Manley, E. R. Thompson, L. C. Fox, S. Yerneni, P. Blombery, G. J. Lieschke, Transient, flexible gene editing in zebrafish neutrophils and macrophages for determination of cell-autonomous functions. *Dis. Model. Mech.* **14**, dmm047431 (2021).

89. J. A. Castro-Mondragon, R. Riudavets-Puig, I. Rauluseviciute, R. B. Lemma, L. Turchi, R. Blanc-Mathieu, J. Lucas, P. Boddie, A. Khan, N. Manosalva Perez, O. Fornes, T. Y. Leung, A. Aguirre, F. Hammal, D. Schmelter, D. Baranasic, B. Ballester, A. Sandelin, B. Lenhard, K. Vandepoele, W. W. Wasserman, F. Parcy, A. Mathelier, JASPAR 2022: The 9th release of the open-access database of transcription factor binding profiles. *Nucleic Acids Res.* **50**, D165–D173 (2022).

90. T. Jowett, L. Lettice, Whole-mount in situ hybridizations on zebrafish embryos using a mixture of digoxigenin- and fluorescein-labelled probes. *Trends Genet.* **10**, 73–74 (1994).